Conductive Polymer Films as Electrodes in Organic Solar Cells

by

© John Healey

A thesis submitted in partial fulfilment of

the requirements for the degree of

Bachelor of Science (Honours)

Department of Physics and Physical Oceanography

Memorial University of Newfoundland

April 2020

St. John's Newfoundland

Contents

Abstract

As predictions on the future of Earth's climate have grown increasingly dire, it has become clear that a transition from fossil fuels to renewable energy sources is necessary. Organic solar cells (OSCs) are an emerging photovoltaics technology with several advantages over traditional silicon-based cells including low manufacturing cost, high flexibility, and high transparency. However, most OSC architectures still use inorganic Indium Tin Oxide (ITO) as the anode material, increasing costs and reducing sustainability of the manufacturing process. In this study, the conductive polymer poly(3,4-ethylenedioxythiophene) polystyrene sulfonate (PEDOT:PSS) is investigated as an alternative anode material for OSCs, and its performance as an anode is optimized. It was found that ITO possesses a higher transmittance in the solar spectrum than PEDOT:PSS, and that ITO synergizes better with existing standards such as the P3HT:PCBM active layer material. Electrical tests were inconclusive, so it is left to future work to determine conclusively the suitability of PEDOT:PSS as an anode material for OSCs.

Acknowledgements

I would like to thank Dr. Qiying Chen and Dr. Jolanta Lagowski for lending me their patience and expertise throughout this project. Without their guidance, this never would have been possible. I would also like to thank Dr. Liqiu Men for her assistance in the lab. I would like to thank Dr. Mike Morrow for allowing me to perform supplementary experiments using his equipment. I must also thank Dr. Stephanie Curnoe for ensuring that I stay on track and complete my milestones on schedule.

I would like to thank my friends for their encouragement and emotional support, and for helping me find joy in my struggles. Finally, I would like to thank my parents for supporting me throughout this project and beyond.

List of Figures

Chapter 1

Introduction

1.1 Photovoltaics

Solar cells operate on the basis of the photovoltaic effect, in which electric current is generated through the absorption of light. This effect was first demonstrated by Becquerel in 1839 using an electrochemical cell, and has been heavily researched ever since as a method of generating clean electricity from the essentially endless stream of energy provided by the sun. The first practical photovoltaic device was invented by Bell Labs in 1954, when Chapin, Fuller and Pearson created the first silicon solar cell, which was capable of powering a simple electrical device for several hours a day [1]. As shown in Figure 1.1, the Power Conversion Efficiencies (PCEs) of solar cell devices have gradually increased over the past 50 years, aided by the significant amount of effort gone into improving the electrical properties of silicon for use in microelectronics [2]. However, due to the high demand for silicon, several new types of photovoltaic devices have emerged recently to alleviate the reliance on silicon,

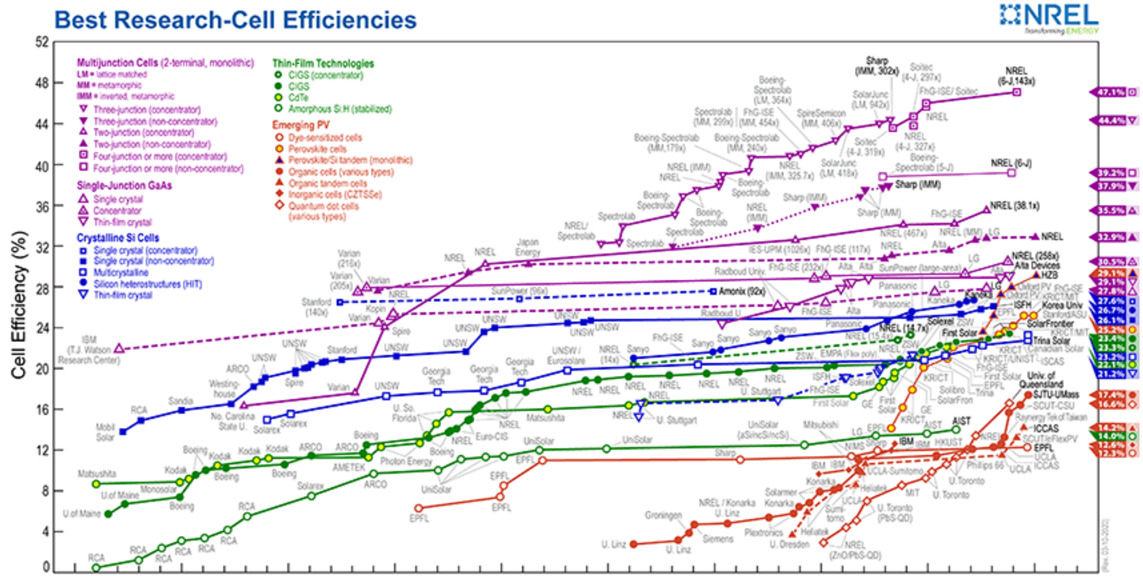

Figure 1.1: Record solar cell efficiencies by year [3].

including Organic Solar Cells (OSCs).

When a photon is absorbed, it excites an electron into a higher-energy state. The excited electron travels through the device to the cathode, where it is collected to generate current. OSCs are distinguished from traditional silicon-based devices by the use of an organic substance (usually a conductive polymer) rather than silicon as the material in which excitation takes place [4]. OSCs benefit from an inexpensive, simple, and environmentally-friendly manufacturing process [5]. They may also be used in novel applications such as wearable technologies and solar windows, since they can easily be made to be flexible [6] and transparent [7]. However, OSCs have also suffered from poor stability in ambient conditions, and a generally low efficiency compared to their inorganic counterparts. The record efficiency for an OSC at the time of writing is 17.4%, while for a silicon solar cell, the record efficiency is 47.1% [3].

The exact mechanisms at work in OSCs are discussed below.

1.2 Organic Solar Cells

1.2.1 Excitation

As mentioned above, the absorption of a photon by a solar cell causes an electron to be excited into a higher-energy state. This process takes place in the **active layer** of the cell. To facilitate excitation and collection, the active layer in an OSC is comprised of two different types of materials: an electron donor and an electron acceptor. Light is absorbed by the donor material, exciting an electron from the material's Highest Occupied Molecular Orbital (HOMO) to its Lowest Unoccupied Molecular Orbital (LUMO). The energy gap between the HOMO and LUMO is known as the band gap, E_G, and is an essential concept in photovoltaics. If the photon does not have enough energy to excite an electron from the HOMO to the LUMO, it is not absorbed by the active layer, and will either be absorbed by one of the other layers of the cell, or will simply pass through the cell. If the photon has more energy than that required to excite the electron, $E_P > E_G$, then the excess energy is transferred from the electron to its surroundings in a process known as thermal relaxation [1], as it settles down into the LUMO.

1.2.2 Diffusion

When an electron is excited to the LUMO of the donor material, the resulting absence of an electron in the HOMO of this material is known as a hole. Since the hole is the embodiment of the absence of an electron, it is considered to have a positive charge. Thus, the electron and hole undergo Coulombic attraction to one another. This attraction makes the electron want to return to the HOMO of the donor material to recombine with the hole, which is undesirable since the electron can only be transferred to the cathode to create electric current if it is in the excited state. The energy holding the electron and hole together is known as the exciton binding energy, since the electron-hole pair is known as an exciton. This energy is very high in OSCs compared to their inorganic counterparts, and is a large contributor to the generally poor efficiency of OSCs [8]. In order to extract the electron and hole from the exciton, the exciton must first move to a donor-acceptor interface.

Once an exciton is generated, it will move a certain distance through the active layer before the electron and hole that make up the exciton recombine. This distance is a property of the materials that make up the active layer, and is known as the exciton diffusion length. If the exciton reaches an interface between the donor and acceptor materials before recombining, the electron and hole may be extracted and put to use. Otherwise, the electron will relax to the HOMO of the donor and any potential power generation from that exciton will be lost. The original OSCs used a bilayer structure in which the donor and acceptor materials were separated in two adjacent layers, as shown in Figure 1.2. Having only one interface between the donor and acceptor materials is very inefficient, since it means that all of the generated excitons have to diffuse to just one specific interface. Many would be created at a distance greater than the diffusion length from the interface, so these would all be lost to recombination.

The solution to this problem used in most modern OSCs is the Bulk Hetero-

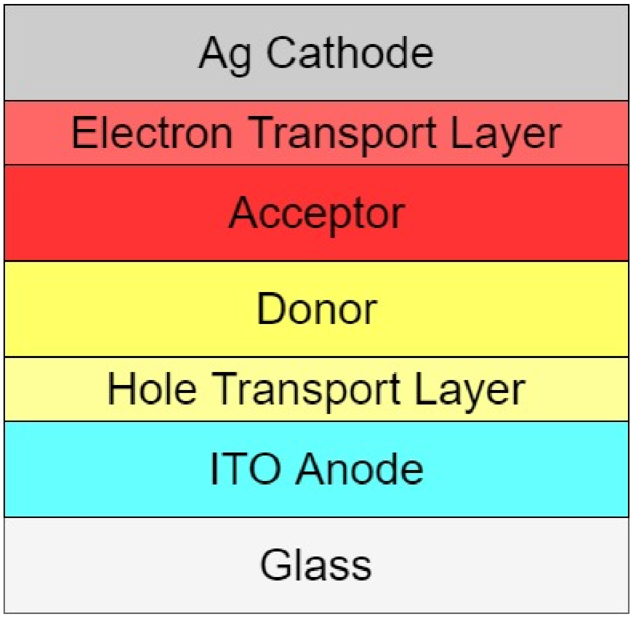

Figure 1.2: A typical Bilayer OSC architecture. Recreated from [2].

junction (BHJ) active layer, in which the donor and acceptor materials are blended together to form one single layer. Within this one layer are dispersed many donor-acceptor interfaces, meaning that generated excitons need to travel much less distance before they encounter an interface, so the recombination rate is greatly reduced. A schematic diagram of an OSC using a typical BHJ active layer is shown in Figure 1.3

1.2.3 Extraction

The donor and acceptor materials are chosen so that their energy levels align as shown in Figure 1.4. The LUMO of the donor material has a higher energy than that of the acceptor material, such that an electron excited in the donor will want to move to the acceptor when it reaches the interface.

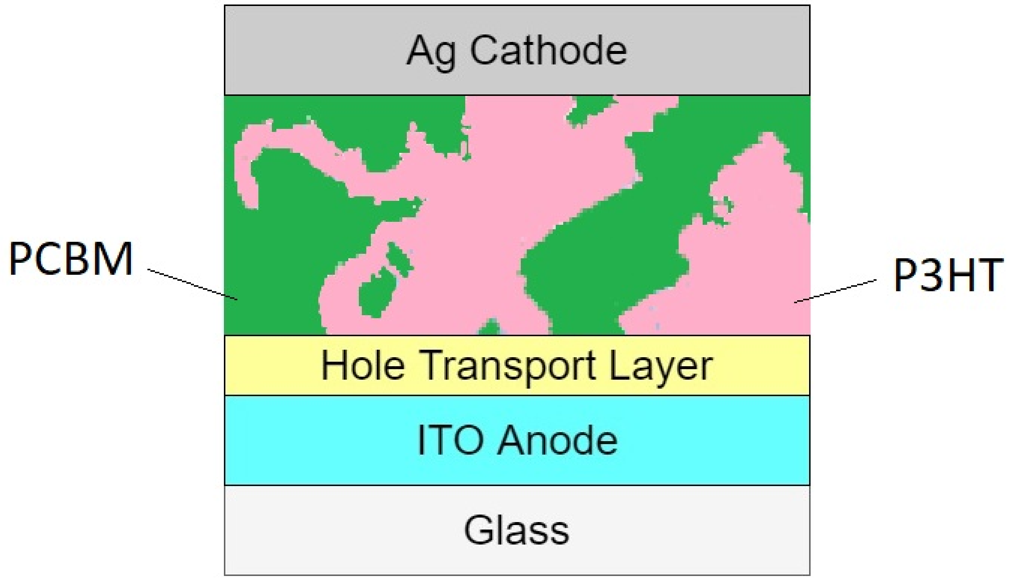

Figure 1.3: A typical Bulk Heterojunction (BHJ) OSC architecture. Recreated from [9].

1.2.4 Transport

Once the exciton has been split at the interface, the constituent electron and hole are transported to the cathode and anode of the device, respectively. By selecting materials with different work functions for the anode and cathode, a net electric field is established throughout the device corresponding to the potential difference between the electrodes. This electric field points from the cathode to the anode, and therefore drives electrons to the cathode and holes to the anode, leading to the generation of electric current. The recombination discussed earlier - called radiative recombination because upon relaxation of the electron to the HOMO, a photon is emitted - is no longer a possibility. However, charges can still be trapped in film defects and trap states, which is why film quality is of such high importance [11].

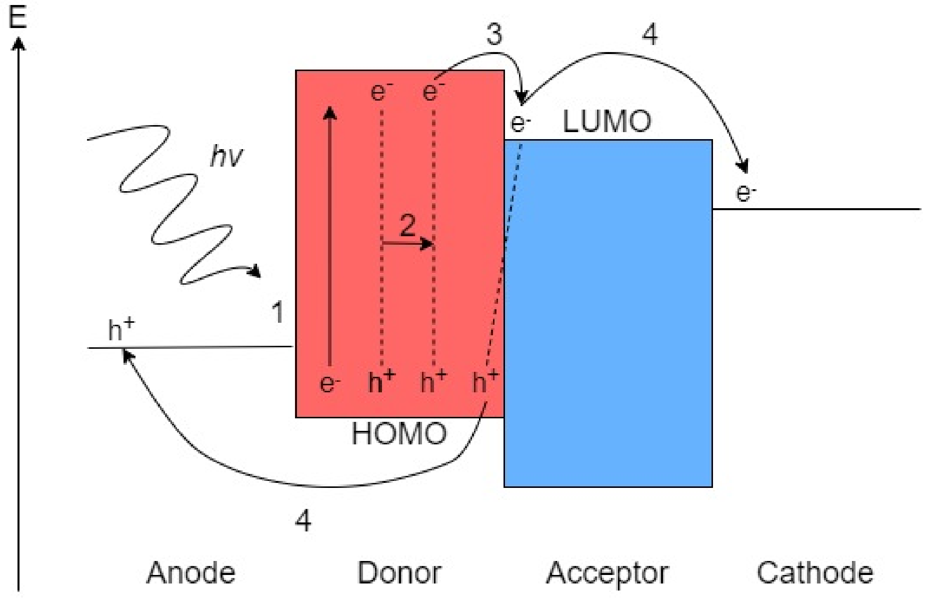

Figure 1.4: A diagram showing the energy levels of the donor and acceptor materials in the active layer of an OSC, and the process of photocurrent generation. **(1)** A photon of energy $h\nu$ is absorbed by the donor material, exciting an electron e^- from the HOMO to the LUMO of this material. **(2)** The resulting exciton diffuses to the donor-acceptor interface. **(3)** The excited electron moves to the LUMO of the acceptor material, while the hole remains in the HOMO of the donor. **(4)** The electron is transported to the cathode, and the hole to the anode. Recreated from [10].

1.3 Current Work

The main problems facing OSCs are their low efficiency and poor stability, so naturally, most current research on this technology focuses on these two issues. Due to the wide variety of available organic semiconducting materials, studies often involve the addition or replacement of a novel material into an existing OSC architecture [12]. In this study, the suitability of organic poly(3,4-ethylenedioxythiophene) polystyrene sulfonate (PEDOT:PSS) as a replacement for inorganic Indium Tin Oxide (ITO) as the anode material in OSCs is investigated. Through this replacement, the manufacturing process for OSCs would be made simpler, less expensive, and more environmentally-friendly [5]. While efficiency and stability are heavily researched areas, these practical manufacturing concerns are rarely taken into account. One must consider, however, that silicon is such a ubiquitous material that its manufacturing process has become extremely optimized over the past 50 years. If OSCs are going to compete with silicon-based cells, their fabrication techniques must also be very streamlined, which can only be accomplished through research on the areas listed above.

PEDOT:PSS was shown to work as the anode material in OSCs in a 2008 study [13], but the resulting cells showed very low efficiencies, so were mostly dismissed. However, PEDOT:PSS is a heavily-researched material [14, 15], so in the years since this study, the electrical and optical properties of PEDOT:PSS have been significantly improved as new types have been synthesized [16]. It is therefore expected that devices with PEDOT:PSS anodes will now be able to achieve a higher performance than in 2008, and thereby remain competitive with current OSC architectures.

This study began with a computational investigation of the optical properties of OSCs using ITO and PEDOT:PSS anodes. Experiments were then performed to confirm the computational results and to obtain additional metrics for solar cell performance. In Chapter 2, the modelling methods used for the computational portion of this study are discussed in detail. In Chapter 3, the experimental setup for sample fabrication and characterization is described. In Chapter 4, the computational and experimental results are presented and discussed. Finally, in Chapter 5, an overview of the significant results is presented, and potential future work is discussed.

Chapter 2

Computational Modelling

In this chapter, Transfer Matrix Formalism - the computational modelling technique used in this project - is developed, following and expanding upon the derivation given in [17]. This formalism is heavily based on the Fresnel Equations, so a brief derivation is given for these as well. To implement this model, wavelength-dependent values of refractive index and extinction coefficient are required for each of the materials used in the cell. The values used here are taken from a study by Burkhard, Hoke and McGehee [18], who made their data available to the public.

2.1 Transfer Matrix Formalism

To understand TMF, consider light approaching a single interface from both sides, as shown in Figure 2.1. E_{fn} is the amplitude of a wave moving "forwards" in layer n, and E_{bn} is the amplitude of a wave moving "backwards" in layer n. We can deduce that each component moving *away* from the interface is the result of the addition of two interfering amplitudes. For example, the component moving backwards in Layer 1,

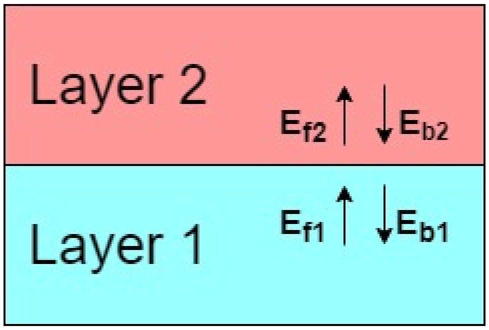

Figure 2.1: Light at each side of an interface. Modified from Byrnes, Steven [17].

E_{b1}, is composed of the part of E_{f1} that gets reflected from the interface and the part of E_{b2} that is transmitted through the interface. Letting r_{ab} and t_{ab} be the reflection and transmission coefficients going from layer a to layer b, we get:

$$E_{b1} = E_{f1} r_{12} + E_{b2} t_{21}. \tag{2.1}$$

Similarly, the component moving forwards in Layer 2 is composed of the part of E_{f1} that is transmitted through the interface, and the part of E_{b2} that is reflected at the interface:

$$E_{f2} = E_{f1} t_{12} + E_{b2} r_{21}. \tag{2.2}$$

This idea can be extended by considering a device with more than two layers, as shown in Figure 2.2. For simplicity, let v represent a forward-moving component and w represent a backward-moving component.

In the case of multiple interfaces, v is strictly defined as the forward-moving amplitude *immediately after* leaving an interface, and w as the backward-moving amplitude *immediately before* hitting an interface. This is a more consistent system than in the previous case, in which E_{f1} was the value immediately before hitting the interface and E_{f2} was the value immediately after. In this new system, the

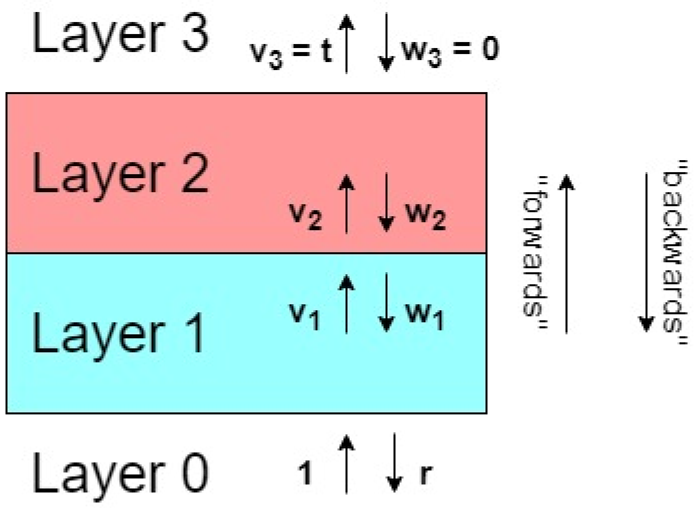

Figure 2.2: Light travelling through a multilayer device. Recreated from [17].

modification of the amplitude as the light travels through the device is taken into account. For example, whereas in the previous system E_{f2} was simply the sum of the transmitted part of E_{f1} and the reflected part of E_{b2}, consider now the fact that the forward-moving light in Layer 1 (now called v_1) must travel all the way through Layer 1 in order to reach the interface. By travelling through this layer, the amplitude is modified by $e^{i\delta_n}$, such that:

$$v_2 = (v_1 e^{i\delta_1})t_{12} + w_2 r_{21} \tag{2.3}$$

where

$$\delta_n \equiv (\text{thickness of layer } n) \times (k \text{ for the forward-travelling wave in layer } n). \tag{2.4}$$

More generally,

$$v_{n+1} = (v_n e^{i\delta_n})t_{n,n+1} + w_{n+1} r_{n+1,n}. \tag{2.5}$$

Similarly, the part of w_2 that is transmitted must travel through Layer 1 in order to contribute to w_1, as must the part of $v_1 e^{i\delta_1}$ that is reflected. So, the expression for

w_1 is:

$$w_1 = (w_2 t_{21})e^{i\delta_1} + ((v_1 e^{i\delta_1})r_{12})e^{i\delta_1}. \tag{2.6}$$

More generally,

$$w_n = (w_{n+1} t_{n+1,n})e^{i\delta_n} + ((v_n e^{i\delta_n})r_{n,n+1})e^{i\delta_n}. \tag{2.7}$$

For the purposes of creating matrices to represent these relations, expressions of v_n and w_n in terms of v_{n+1} and w_{n+1} are desirable. For v_n, Eq. 2.5 is rearranged to get:

$$v_n = (\frac{1}{t_{n,n+1}})(e^{-i\delta_n})v_{n+1} - (\frac{1}{t_{n,n+1}})(r_{n+1,n})(e^{-i\delta_n})w_{n+1}. \tag{2.8}$$

For w_n, the process is a bit more complicated. First, substitute this new expression for v_n (or $v_n e^{i\delta_n}$ for simplicity) into Eq. 2.7:

$$w_n = (w_{n+1} t_{n+1,n})e^{i\delta_n} + ((v_n e^{i\delta_n})r_{n,n+1})e^{i\delta_n}$$

$$w_n = (w_{n+1} t_{n+1,n})e^{i\delta_n} + \tfrac{r_{n,n+1}}{t_{n,n+1}}(v_{n+1} - w_{n+1} r_{n+1,n})e^{i\delta_n}$$

$$w_n = (\tfrac{r_{n,n+1}}{t_{n,n+1}})(e^{i\delta_n})v_{n+1} + (t_{n+1,n} - \tfrac{r_{n,n+1}}{t_{n,n+1}} r_{n+1,n})(e^{i\delta_n})w_{n+1}.$$

Then, two identities derived from the Fresnel Equations (Eq. 2.38, derived later) can be used:

$$t_{a,b} - r_{a,b} = 1 \tag{2.9}$$

and

$$t_{a,b} t_{b,a} - r_{a,b} r_{b,a} = 1. \tag{2.10}$$

Eq. 2.9 is applied to the coefficient of the v_{n+1} term to get:

$$(\frac{r_{n,n+1}}{t_{n,n+1}})e^{i\delta_n} = (1 - \frac{1}{t_{n,n+1}})e^{i\delta_n}. \tag{2.11}$$

Eq. 2.10 is applied to the coefficient of the w_{n+1} term to get:

$$(t_{n+1,n} - \tfrac{r_{n,n+1}}{t_{n,n+1}} r_{n+1,n})(e^{i\delta_n})$$

$$= \tfrac{1}{t_{n,n+1}}(t_{n+1,n}t_{n,n+1} - r_{n,n+1}r_{n+1,n})e^{i\delta_n}$$

$$= (\tfrac{1}{t_{n,n+1}})e^{i\delta_n}$$

Substituting these expressions back into the equation for w_n produces:

$$w_n = (1 - \frac{1}{t_{n,n+1}})(e^{i\delta_n})v_{n+1} + (\frac{1}{t_{n,n+1}})(e^{i\delta_n})w_{n+1}. \tag{2.12}$$

By examining the equations for v_n and w_n side-by-side, the development of the matrix formalism becomes clear:

$$v_n = (\tfrac{1}{t_{n,n+1}})(e^{-i\delta_n})v_{n+1} - (\tfrac{1}{t_{n,n+1}})(r_{n+1,n})(e^{-i\delta_n})w_{n+1}$$

$$w_n = (1 - \tfrac{1}{t_{n,n+1}})(e^{i\delta_n})v_{n+1} + (\tfrac{1}{t_{n,n+1}})(e^{i\delta_n})w_{n+1}.$$

This relationship can be expressed as:

$$\begin{bmatrix} v_n \\ w_n \end{bmatrix} = M_n \begin{bmatrix} v_{n+1} \\ w_{n+1} \end{bmatrix} \tag{2.13}$$

where

$$M_n = \begin{bmatrix} (\tfrac{1}{t_{n,n+1}})e^{-i\delta_n} & -(\tfrac{1}{t_{n,n+1}})(r_{n+1,n})e^{-i\delta_n} \\ (1 - \tfrac{1}{t_{n,n+1}})e^{i\delta_n} & (\tfrac{1}{t_{n,n+1}})e^{i\delta_n} \end{bmatrix}. \tag{2.14}$$

Using the same identities given above, as well as $r_{a,b} = -r_{b,a}$ (which also comes from the Fresnel Equations), the terms at positions $1, 2$ and $2, 1$ can be rewritten as:

$$M_n = \begin{bmatrix} \frac{1}{t_{n,n+1}} e^{-i\delta_n} & \frac{1}{t_{n,n+1}} (r_{n,n+1}) e^{-i\delta_n} \\ \\ \frac{1}{t_{n,n+1}} (r_{n,n+1}) e^{i\delta_n} & \frac{1}{t_{n,n+1}} e^{i\delta_n} \end{bmatrix}. \tag{2.15}$$

The $\frac{1}{t_{n,n+1}}$ terms can be factored out to get:

$$M_n = \frac{1}{t_{n,n+1}} \begin{bmatrix} e^{-i\delta_n} & e^{-i\delta_n} r_{n,n+1} \\ \\ e^{i\delta_n} r_{n,n+1} & e^{i\delta_n} \end{bmatrix}. \tag{2.16}$$

This matrix can be expressed as the multiplication of two simple matrices:

$$M_n = \begin{bmatrix} e^{-i\delta_n} & 0 \\ \\ 0 & e^{i\delta_n} \end{bmatrix} \begin{bmatrix} 1 & r_{n,n+1} \\ \\ r_{n,n+1} & 1 \end{bmatrix} \frac{1}{t_{n,n+1}}. \tag{2.17}$$

This is the heart of the Transfer Matrix Formalism, where the Layer Matrices (L_n) and Interface Matrices ($I_{n,n+1}$) come from Eq. 2.17:

$$L_n = \begin{bmatrix} e^{-i\delta_n} & 0 \\ \\ 0 & e^{i\delta_n} \end{bmatrix}. \tag{2.18}$$

$$I_{n,n+1} = \begin{bmatrix} 1 & r_{n,n+1} \\ \\ r_{n,n+1} & 1 \end{bmatrix} \frac{1}{t_{n,n+1}}. \tag{2.19}$$

The above equations were coded using Python in Jupyter Notebook (see Appendix A).

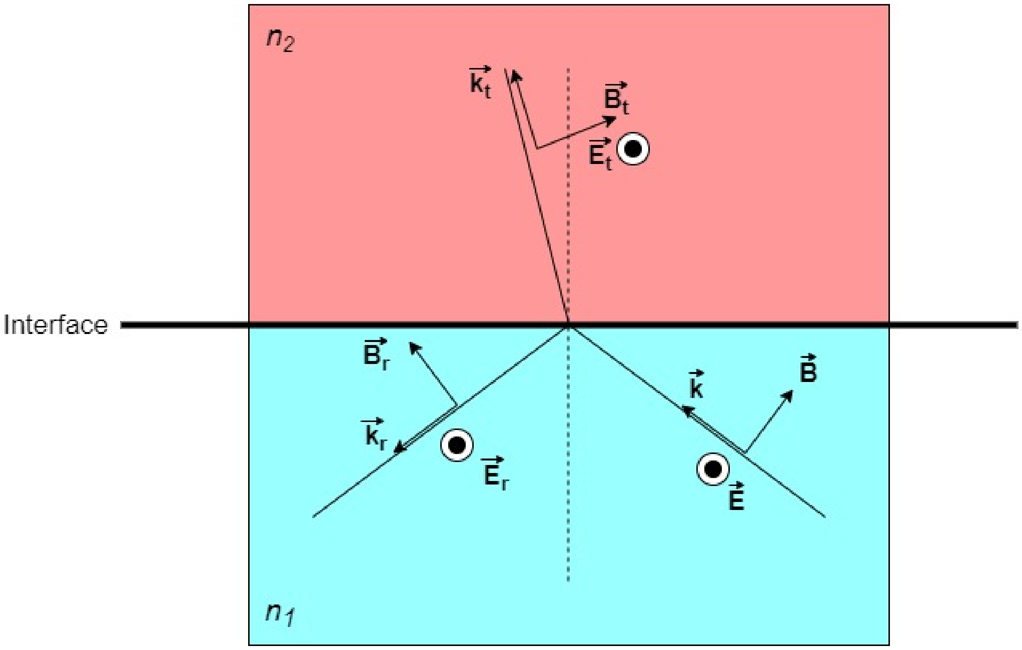

Figure 2.3: Incident, reflected and transmitted electromagnetic waves at an interface. Recreated from [19].

2.2 Fresnel Coefficients

To derive the expressions for the Fresnel coefficients, light at an interface is treated as an electromagnetic wave. It will be assumed that the light propagates in the direction of k such that E is perpendicular to the plane of incidence, as shown in Figure 2.3. This mode of polarization is called the *transverse electric* (TE) mode. The *transverse magnetic* mode could just as easily be considered, and would produce analogous results. Figure 2.3 shows a wave incident on a plane interface, as well as the reflected and transmitted (refracted) waves. The incident wave can be expressed as

$$E = E_0 e^{i(k \cdot r - \omega t)} \tag{2.20}$$

and the reflected and transmitted waves as

$$E_r = E_{0r} e^{i(k_r \cdot r - \omega_r t)} \tag{2.21}$$

and

$$E_t = E_{0t} e^{i(k_t \cdot r - \omega_t t)} \tag{2.22}$$

respectively. Since all three waves exit the interface simultaneously, their phases must be equal:

$$(k \cdot r - \omega t) = (k_r \cdot r - \omega_r t) = (k_t \cdot r - \omega_t t). \tag{2.23}$$

At $r = 0$,

$$-\omega t = -\omega_r t = -\omega_t t \tag{2.24}$$

or

$$\omega = \omega_r = \omega_t, \tag{2.25}$$

so the frequencies of all three waves are equal.

At $t = 0$,

$$k \cdot r = k_r \cdot r = k_t \cdot r. \tag{2.26}$$

Given that the dot product of two vectors k and r is the length of the projection of k onto r multiplied by the length of r, the first two terms of this equation can be rewritten as

$$kr \sin\theta = k_r r \sin\theta_r. \tag{2.27}$$

In this particular case, since the incident and reflected waves travel in the same medium, their wavelengths are identical and $k = k_r$. Therefore,

$$\sin\theta = \sin\theta_r \tag{2.28}$$

and

$$\theta = \theta_r, \tag{2.29}$$

which is the law of reflection. Similarly, for the last two terms of Eq. 2.26,

$$k_r r \sin\theta_r = k_t r \sin\theta_t. \tag{2.30}$$

Given that the frequencies of the three waves are equal (Eq. 2.25), it must be true for the reflected wave that $k_r = \omega/v_r$ and, from the definition of the refractive index, $k_r = n_1\omega/c$. Similarly, for the transmitted wave, $k_t = n_2\omega/c$. Substituting these into Eq. 2.30,

$$n_1 \sin\theta_r = n_2 \sin\theta_t, \tag{2.31}$$

which is the law of refraction.

These results are then extended using boundary conditions from Maxwell's equations, which will be used without proof. The boundary conditions require that the components of the electric and magnetic fields *parallel* to the boundary plane be continuous as the boundary is crossed. As can be seen in Figure 3, this includes all components of the electric field, as well as the x-component of the magnetic field. Therefore,

$$E + E_r = E_t \tag{2.32}$$

and

$$B\cos\theta - B_r\cos\theta = B_t\cos\theta_t, \tag{2.33}$$

given $\theta_r = \theta$ - as proven earlier - and the fact that the magnetic field of the reflected wave is in the negative x-direction. Using the relation

$$E = vB = (c/n)B, \tag{2.34}$$

the magnetic fields can be expressed in terms of electric fields: $B = (n_1/c)E$, $B_r = (n_1/c)E_r$, and $B_t = (n_2/c)E_t$. Thus, the following system of equations is obtained:

$$E + E_r = E_t \tag{2.35}$$

$$n_1 E \cos\theta - n_1 E_r \cos\theta = n_2 E_t \cos\theta_t. \tag{2.36}$$

Eliminating E_t:

$$\begin{cases} E + E_r = E_t \\ n_1 E \cos\theta - n_1 E_r \cos\theta = n_2 E_t \cos\theta_t. \end{cases}$$

$$\begin{cases} n_2 E \cos\theta_t + n_2 E_r \cos\theta_t = n_2 E_t \cos\theta_t \\ n_1 E \cos\theta - n_1 E_r \cos\theta = n_2 E_t \cos\theta_t \end{cases}$$

$$E(n_2 \cos\theta_t - n_1 \cos\theta) + E_r(n_2 \cos\theta_t + n_1 \cos\theta) = 0$$

$$E_r(n_2 \cos\theta_t + n_1 \cos\theta) = -E(n_2 \cos\theta_t - n_1 \cos\theta)$$

Then, by definition,

$$r \equiv \frac{E_r}{E} = \frac{-(n_2 \cos\theta_t - n_1 \cos\theta)}{n_2 \cos\theta_t + n_1 \cos\theta} = \frac{n_1 \cos\theta - n_2 \cos\theta_t}{n_1 \cos\theta + n_2 \cos\theta_t}. \tag{2.37}$$

Using the definition of the transmission coefficient and Eq. 2.35,

$$t \equiv \frac{E_t}{E} = 1 + \frac{E_r}{E} = 1 + r. \tag{2.38}$$

Then, substituting in the new expression for r (Eq. 2.37):

$$t = \frac{n_1 \cos\theta + n_2 \cos\theta_t}{n_1 \cos\theta + n_2 \cos\theta_t} + \frac{n_1 \cos\theta - n_2 \cos\theta_t}{n_1 \cos\theta + n_2 \cos\theta_t} = \frac{2 n_1 \cos\theta}{n_1 \cos\theta + n_2 \cos\theta_t}. \tag{2.39}$$

Thus, expressions for the Fresnel reflection and transmission coefficients have been derived for a transverse electric wave at an interface.

Chapter 3

Experimental Setup

In this chapter, the techniques used for sample preparation and characterization are described in detail. The purpose of these experiments is to investigate the optical and electrical properties of PEDOT:PSS as the anode material in an organic solar cell architecture, comparing its performance with that of ITO - a traditional inorganic anode material. Additionally, we seek to optimize the performance of the PEDOT:PSS anode by experimenting with different anode thicknesses.

3.1 Sample Fabrication

The fabrication steps described in this section are based on the work of Ding [20] and Hunt [21].

3.1.1 ITO Anode Samples

The ITO anode samples are those that use a traditional OSC architecture, which includes ITO as the anode material. These devices have five layers, comprising the following structure: Glass/ITO/PEDOT:PSS/P3HT:PCBM/Ag. A structural diagram for these devices is shown in Figure 3.1.

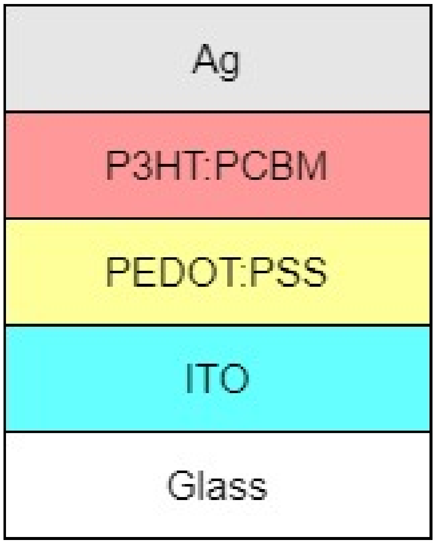

Figure 3.1: Schematic Diagram of an OSC using a traditional architecture.

In order to ensure standardization amongst these cells and to avoid cumbersome vacuum-deposition processes, CB-50IN ITO-coated glass substrates have been purchased from Delta Technologies, Ltd. [22]. The type of PEDOT:PSS used for the hole-transporting buffer layer in these cells is Clevios P VP Al 4083, purchased from H.C. Stark, Inc. [23]. This type was chosen for its high transmission in the solar spectrum [24], which will allow more of the incident light to reach the active layer. The P3HT used in the active layer solution was purchased from Rieke Metals Inc. (catalog number 4002-E). The PCBM was C_{60}PCBM, purchased from Nano-C, Ltd.

The Silver Paint used for the cathode was purchased from Canemco-Marivac, Inc. The ITO anode samples were prepared using the following steps:

1. An ITO-coated glass substrate is rinsed with distilled water, then given a 15 minute sonication in baths of ethanol, then acetone, then distilled water. The substrate is rinsed with distilled water after each bath. The substrate is dried with compressed air then heated on a hot plate at 160 °C for 15 minutes to ensure that there is no liquid remaining.

2. Al 4083 PEDOT:PSS is deposited onto the rinsed ITO-coated glass substrate using spin-coating at 3500 rpm for 60 seconds. The resulting sample is then annealed on a hot plate at 150 °C for 10 minutes.

3. The active layer solution is prepared by mixing P3HT and PCBM at a 1:1 weight ratio, using 1,2-dichlorobenzene as the solvent to achieve a concentration of 10 mg/ml. The solution is stirred overnight using a magnetic stirring rod.

4. The P3HT:PCBM solution is deposited onto the PEDOT:PSS layer by spin-coating at 1000 rpm for 40 seconds. The sample is then annealed on a hot plate at 150 °C for 10 minutes.

3.1.2 PEDOT:PSS Samples

The PEDOT:PSS anode samples are those that replace ITO with PEDOT:PSS as the anode material. These devices have four layers, as follows: Glass/PEDOT:PSS/P3HT:PCBM/Ag. The type of PEDOT:PSS used for the anode layer is Clevios PH 510, purchased from H.C. Stark, Inc. While PH 510 has a lower transmission than Al 4083 in the solar spectrum, it has a much higher conductivity. Since a high conductivity is essential for anode materials, this trade-off is reasonable. The procedure for creating these samples is as follows:

1. A glass substrate is acquired by cutting a 1" x 1" section off of a microscope slide.

2. The substrate is rinsed with distilled water, then given a 15 minute sonication in baths of ethanol, then acetone, then distilled water. The substrate is rinsed with distilled water after each bath. The substrate is dried with compressed air then heated on a hot plate at 160 °C for 15 minutes to ensure that there is no liquid remaining.

3. PH 510 PEDOT:PSS is deposited onto the rinsed glass substrates using spin-coating. Samples are prepared with spin-coating speeds ranging from 1500 to 2500 rpm to get a variety of anode thicknesses, as discussed later. Each sample is spin-coated for 60 s, followed by annealing at 120 °C for 20 minutes.

4. The same P3HT:PCBM solution used for the ITO anode samples is deposited onto the PEDOT:PSS layer by spin-coating at 1000 rpm for 40 seconds. The sample is then annealed on a hot plate at 150 °C for 10 minutes.

3.2 Device Characterization

3.2.1 Optical Characterization

Optical characterization consisted of measuring the transmission spectra of the samples at various stages of the fabrication processes described above. Each time a new layer was applied to a device, its spectrum was taken so that differences in the spectra of the completed devices could be more easily explained. Transmission spectra were measured using a LS-1 Tungsten Halogen Lamp, a USB 4000 Spectrometer, and the SpectraSuite software package - all of which were purchased from Ocean Optics, Inc. The setup for these measurements is shown in Figure 3.2. Light from the UV lamp initially shines directly into the spectrometer, and its spectrum is measured. A sample is then placed in the path of the beam, and the spectrum of the light transmitted through the sample is measured. From this data, the SpectraSuite software calculates the percentage of light that is transmitted through the sample at wavelengths between 400 and 1100 nm - in other words determining the sample's transmission spectrum.

3.2.2 Thickness Measurement

In order to ensure that the PEDOT:PSS anode layers had a thickness similar to that of the ITO anode layers, and to quantitatively determine the relationship between spin-coating speed and film thickness, optical surface characterization was performed. To perform these measurements, the Zygo Nexview Optical Surface Profiler was used. This device uses Coherence Scanning Interferometry (CSI) to characterize the topog-

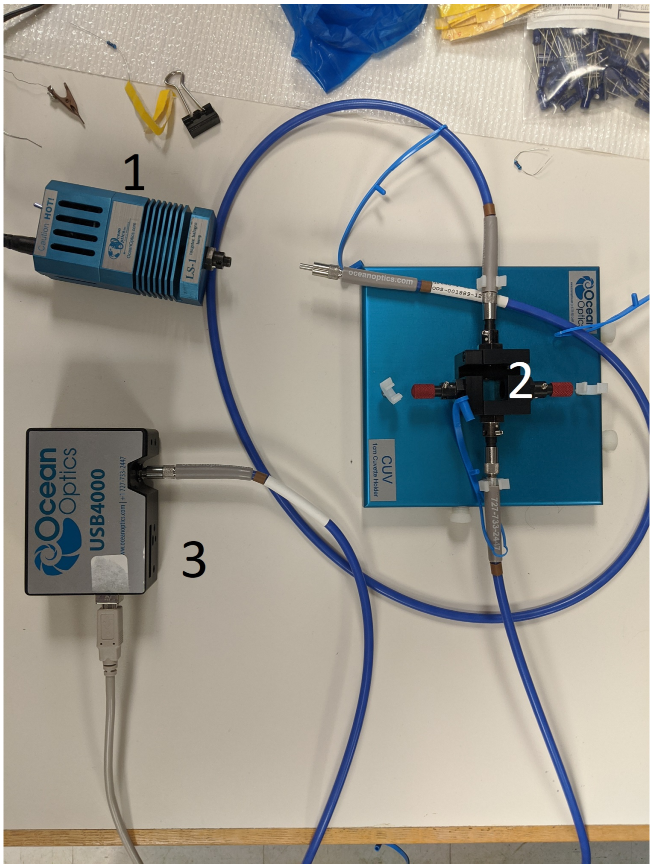

Figure 3.2: Spectrometer Setup for optical characterization. Light from the Halogen lamp (**1**) passes through the sample held in the cuvette holder (**2**) and is collected by the spectrometer (**3**), which sends the transmission data to the PC to be analyzed.

raphy of a given sample. It does not have a built-in way to measure thin-film thickness, but if a scratch is made through the film, the device is able to measure the depth of the scratch, and thereby approximate the thickness of the film.

3.2.3 Electrical Characterization

Electrical characterization consisted of measuring the Current-Voltage (I-V) characteristics of the completed OSC devices under standard solar illumination. The devices are made to be electrically complete by adding the silver cathode on top of the active layer. In order to keep the fabrication process as simple as possible, this was accomplished using conductive silver paint, rather than a complicated and costly vacuum deposition process. Since the application of the cathode would interfere with the optical and surface characterizations, this part of the experiment was carried out last. Once the cathodes were applied to the devices, electrical characterization was carried out using a Newport Oriel 96000 250W solar simulator, a Keithley 2420 SourceMeter, and the LabView software package. The setup for this part of the experiments is shown in Figure 3.3. The solar simulator is designed to emit light that has the same spectrum as sunlight shining on the Earth at a zenith angle of 48.2°. This standard spectrum for testing solar cell efficiency is known as AM 1.5G, and is shown in Figure 3.4.

Under this illumination, the devices produce a photocurrent which is measured at a series of voltages to produce an I-V curve. This is accomplished by connecting the illuminated solar cell to the Keithley, and performing a Voltage sweep while measuring the resulting current. The Keithley is controlled by Labview, which sets the parameters for the voltage sweep, and writes the results to an output file. The I-V curve is a standard metric of a solar cell's performance that can be used to calculate useful quantities such as the device's Power Conversion Efficiency (PCE), which is a measure of how much of the incident radiant energy the device is able to convert into electrical work. An example of a typical solar cell I-V curve obtained using this method can be seen in Figure 3.5.

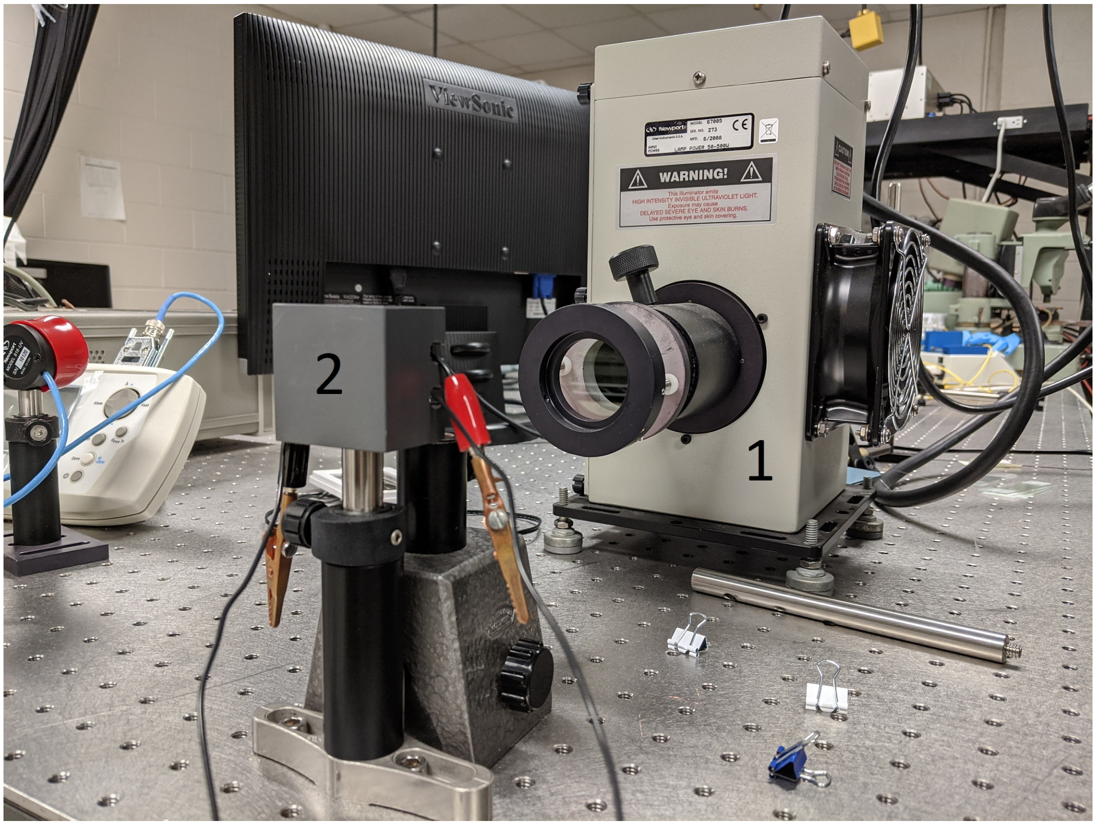

Figure 3.3: Solar simulator used for electrical characterization of OSC devices. Light from the solar simulator (**1**) illuminates the sample in the holder (**2**), and the photocurrent is collected by the red and black leads.

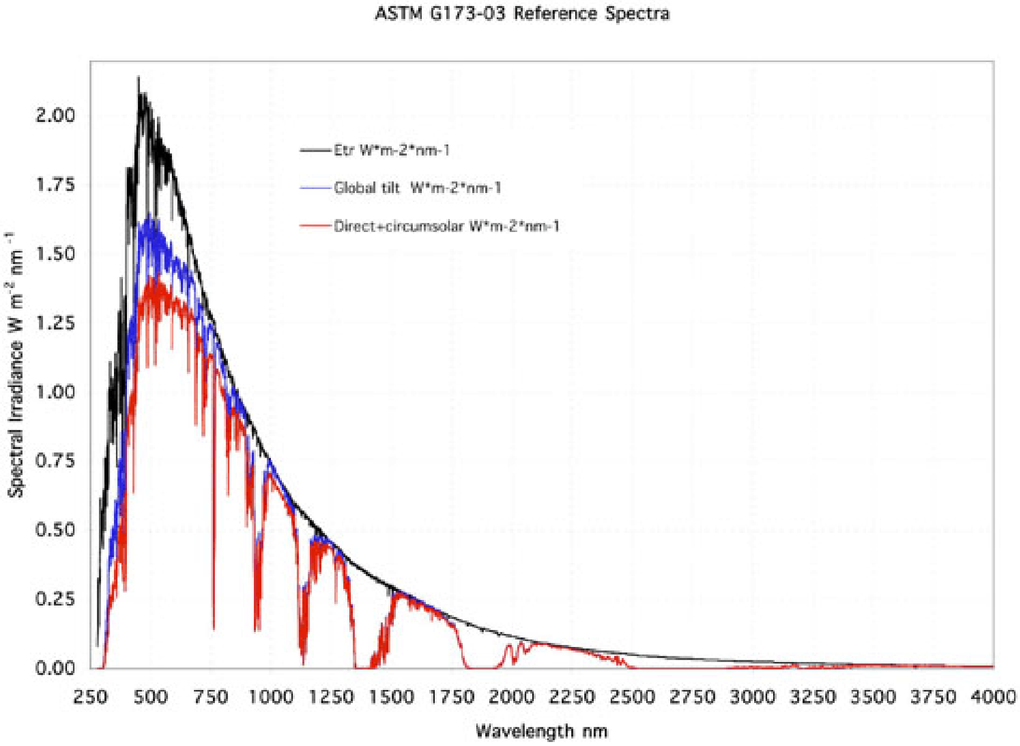

Figure 3.4: AM 1.5 Standard Solar Spectrum from the National Renewable Energy Laboratory [25].

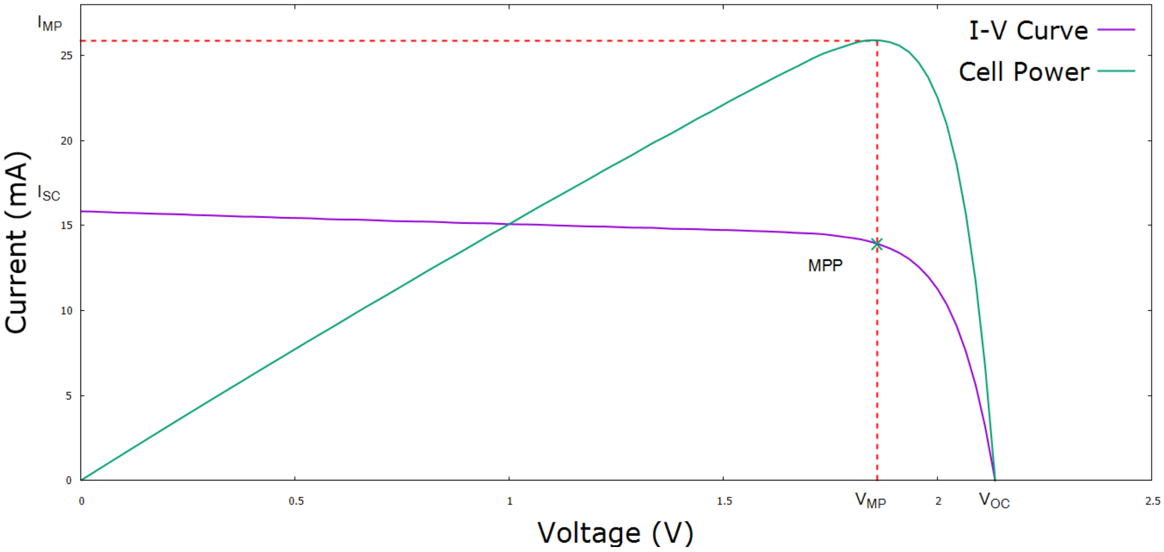

Figure 3.5: Current-Voltage characterization of an inorganic test cell using the methods described in this chapter. Short-Circuit Current (I_{SC}), Open-Circuit Voltage (I_{SC}), Maximum Power Point (MPP), and the Current and Voltage that give the maximum device power.

Chapter 4

Results and Discussion

Substituting the anode material currently used in OSCs from inorganic ITO to an organic material promises to reduce the cost and environmental impact associated with manufacturing OSC devices [26]. In this study, PEDOT:PSS is examined as an organic alternative to ITO. In order to be considered a viable alternative, PEDOT:PSS must be shown to have a transmittance comparable to that of ITO in the solar spectrum (shown in Figure 3.4), so that sunlight may easily pass through it and reach the active layer of the device, where it can be converted into electrical energy. It must also possess a high electrical conductivity so that it is able to effectively harvest holes from the active layer (or hole-transporting buffer layer if one exists) and transport them to the external circuit. In order to determine the extent to which PEDOT:PSS has these properties, this study begins with a computational investigation of the optical properties of an OSC using PEDOT:PSS compared to one using ITO. This is followed by a series of experiments designed to check the computational results, and to further examine the interactions between the adjacent layers in the device.

Rather than just examine the transmission spectra of ITO and PEDOT:PSS individually, complete OSC devices were created using the different anode materials, and the transmission spectra of the multi-layer structures were measured. This way, insight is gained not only on how the anode layers perform individually, but how they effect the optical properties of the device overall. To accommodate transmission measurements, the silver cathode layer will be left off of the devices during optical characterization, since it would not allow light to be transmitted through the back of the devices. The device with the higher transmittance will be said to have the better performance since it means that less light is being absorbed/reflected by the anode. The absorbance of the active layer should be constant throughout all devices, since the active layer of every device uses the same material at the same thickness.

Upon completion of the optical experiments, the devices are characterized electrically through the measurement of their current-voltage properties. From the current-voltage properties, metrics such as PCE can be extracted, providing a more comprehensive test of the viability of PEDOT:PSS as an anode material by incorporating both optical and electrical performance.

In order to provide some insight on how to optimize devices that use PEDOT:PSS as the anode material, all tests on these devices were carried out for a range of PEDOT:PSS thicknesses. In general, as the thickness of the anode layer increases, its transmission decreases, while its electrical properties generally improve [4]. We therefore seek to find a trade-off that provides optimal performance, as characterized by PCE.

Throughout this chapter, any device described as having ITO as the anode material will have the following structure: Glass/ITO(120 ± 100 nm)/PEDOT:PSS(40 ± 5 nm)/P3HT:PCBM(190 ± 10). Any device using PEDOT:PSS as the anode will have the structure: Glass/PEDOT:PSS(Thickness varies)/P3HT:PCBM(190 ± 10 nm). It should be noted that when ITO is used as the anode material, a hole-conducting buffer layer is required. However, when PEDOT:PSS is used, no such layer is required, since PEDOT:PSS is a good conductor of holes (and is, in fact, the material used as the buffer layer in ITO cells). The thickness of the PEDOT:PSS anode layer is measured directly, as described in Section 3.2.2 of this report. The thickness of the ITO-coated glass is taken from the manufacturer [22]. The thicknesses of the PEDOT:PSS buffer layer and the P3HT:PCBM active layer are taken to be the same as those in the work of Hunt [21], since the same materials and conditions were used in preparation of these films.

4.1 Thickness Measurement

Spin-coating is a thin film deposition technique in which the desired material is placed on the center of the substrate in liquid form. The spin-coater then spins the substrate at a very high speed in order to get the liquid to spread across the substrate to form a film. Intuitively, the faster the sample is spun, the thinner the resulting film will be. By measuring the thicknesses of the films prepared using different spin-coating speeds, we can gain more insight into the dependence of film thickness on spin-coating speed. This measurement is also important for ensuring that the thicknesses of our prepared PEDOT:PSS anodes are comparable to that of the purchased ITO anodes. The results of this investigation are shown in Figure 4.1.

As expected, film thickness decreases significantly with increasing spin-coating speed. It is also worth noting that the uncertainty of the thickness measurements tends to decrease with increasing spin-coating speed. The faster the samples are spun, the more uniform the thickness of the resulting film will be [27]. It is therefore logical that the corresponding thickness measurement would have a lower associated uncertainty. The purchased ITO anodes have thicknesses of 140 ± 20 nm, so the thicknesses of the PEDOT:PSS anodes using these spin-coating speeds are sufficiently similar to those of the ITO anodes.

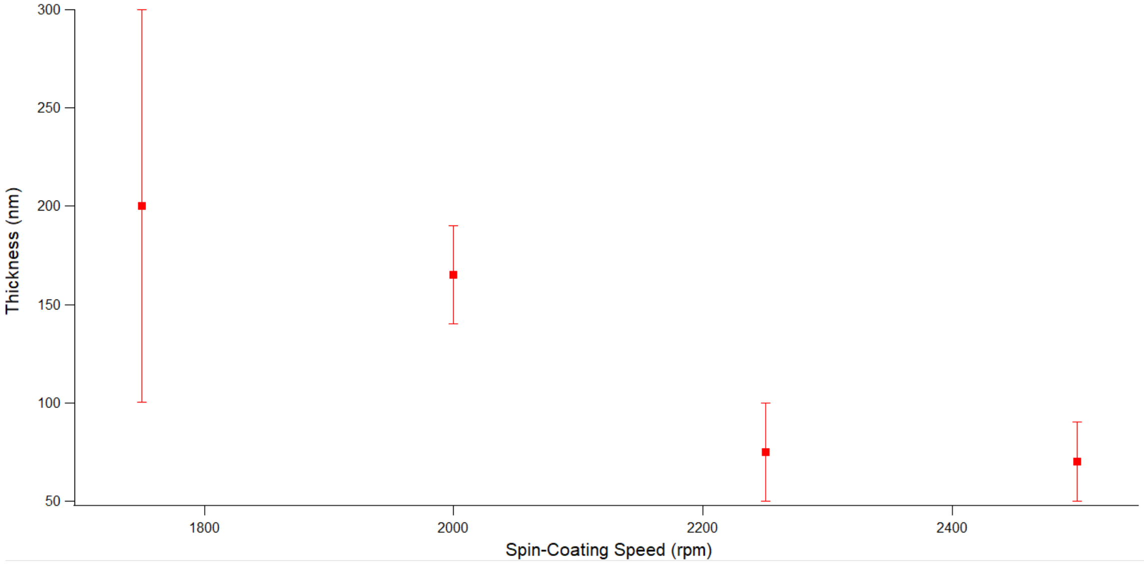

Figure 4.1: Measured thicknesses of PEDOT:PSS films prepared using various spin-coating speeds.

4.2 Modelling Transmission Spectra

Using the Transfer Matrix Formalism described in Chapter 2 of this report, the transmission spectra of an OSC device using ITO as the anode material, and one using PEDOT:PSS as the anode material, were calculated. The results of these calculations are displayed in Figure 4.2. The transmission of the PEDOT:PSS cell is comparable to that of the ITO cell at the lower end of the spectrum, but begins to fall off around 630 nm. The solar spectrum peaks around 600 nm, so this behaviour is not ideal, but the difference in transmission is small enough to warrant further investigation of PEDOT:PSS as a potential anode material.

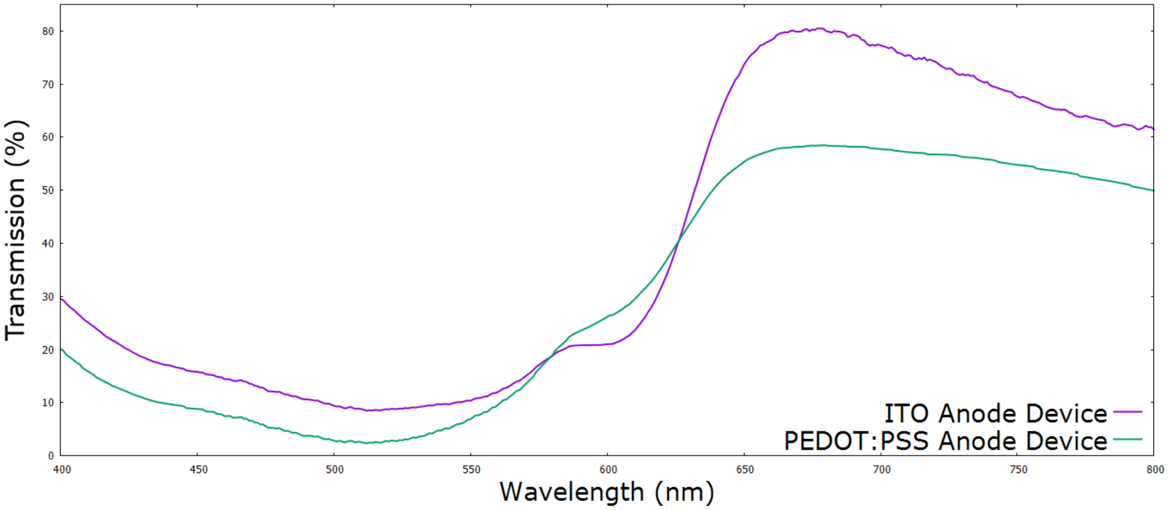

Figure 4.2: Comparison of the modelled transmission spectra of a device with an ITO anode (130 nm) and one with a PEDOT:PSS anode (165 nm).

The thickness of the PEDOT:PSS anode layer in this first simulation is 165 nm. As mentioned above, decreasing the thickness of a film should increase its transmittance.

This dependence is investigated for the PEDOT:PSS anode, as shown in Figure 4.3. The modelled spectra follow the expected behaviour, with transmission increasing across the spectrum with decreasing film thickness. The devices with the thinnest anodes of 70 and 75 nm had a 33% higher transmission than the device with the thickest anode of 200 nm at wavelengths above 630 nm. This significant optical advantage is likely balanced by a lower conductivity, so further testing is required to determine the optimal PEDOT:PSS thickness to be used. However, this simulation increases confidence in the model, and provides an estimation of the dependence of transmittance on film thickness.

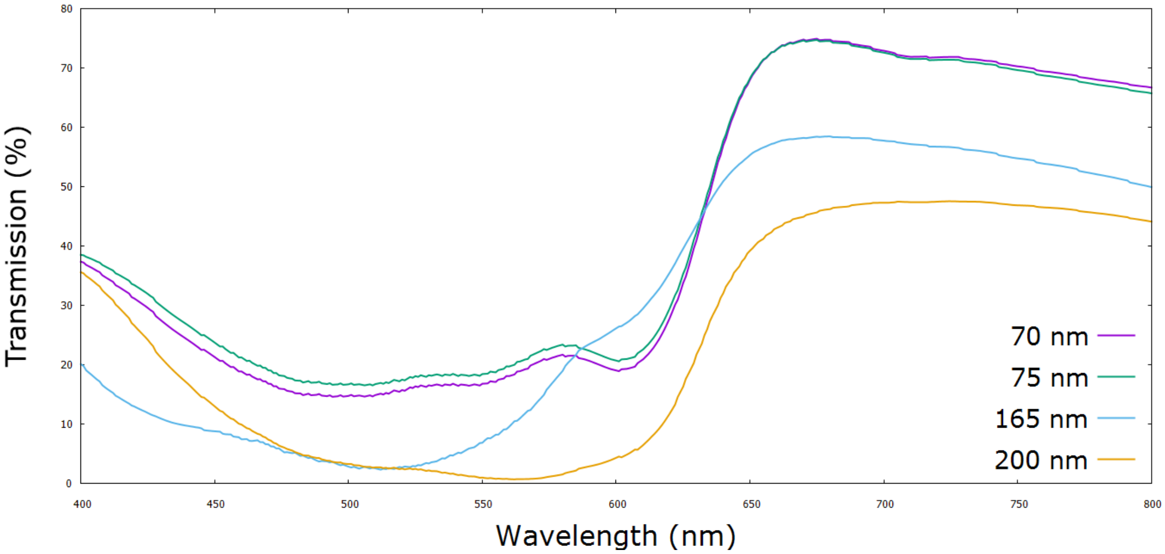

Figure 4.3: Modelled transmission spectra of devices using PEDOT:PSS anodes of different thicknesses.

4.3 Measuring Transmission Spectra

4.3.1 Checking the Model

In order to check the validity of the computational model being used, devices were fabricated with the same structures as the devices being modelled. The transmission spectra of these devices were collected using the setup described in Section 3.2.1 of this report. A comparison of the modelled and measured transmission spectra of two OSC devices is shown in Figure 4.4. While there is a fairly large discrepancy (30% at some wavelengths) between the computational and experimental results for the device with the PEDOT:PSS anode, the overall behaviour of the spectra is consistent between the two. The transmission is decreasing over the wavelength range of 400-525 nm, then increasing from 525-625 nm, then decreasing again over the rest of the spectrum. The large discrepancy is likely due to large variance in the PEDOT:PSS film thickness. This is a common problem encountered when spin-coating is used for film deposition [27], and is not seen for the device with the ITO anode, since this anode was applied using vacuum deposition.

To compensate for thickness inconsistencies in the PEDOT:PSS films, three transmission measurements are taken for each sample, with the light shining through a different part of the sample during each trial. These trials are then averaged to produce a single transmission spectrum for the sample. The experimentally-obtained spectrum in Figure 4.4(a) is an example of a spectrum obtained using this procedure.

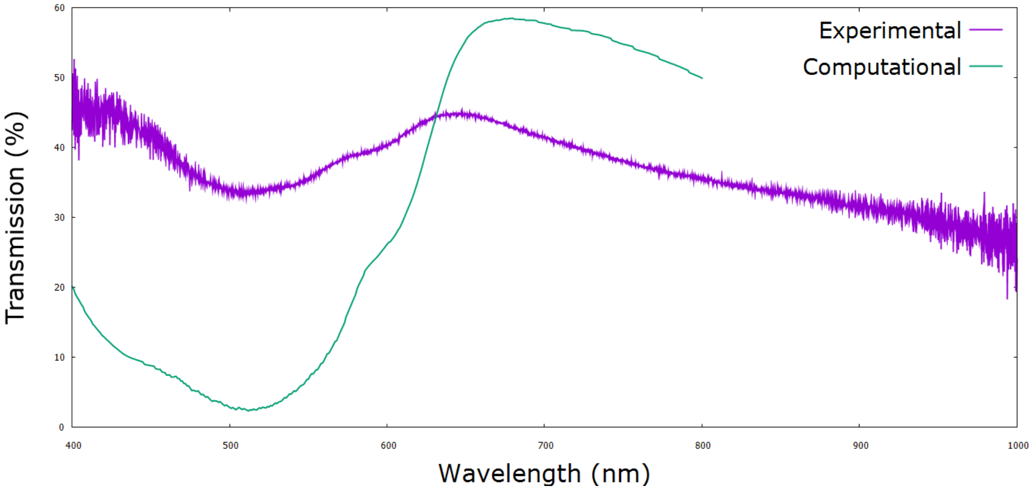

(a) Glass/PEDOT:PSS/P3HT:PCBM

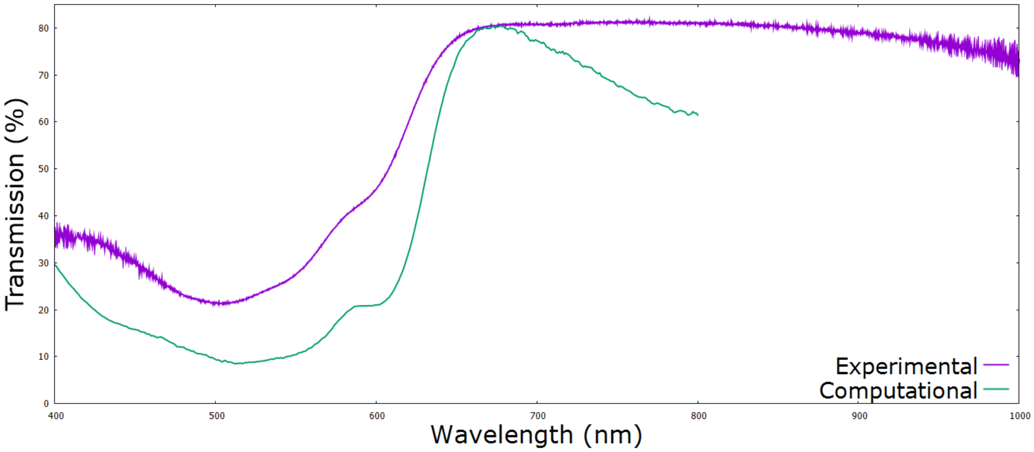

(b) Glass/ITO/PEDOT:PSS/P3HT:PCBM

Figure 4.4: Comparison of the modelled and experimentally determined transmission spectra of an OSC device with a PEDOT:PSS with a thickness of 165 nm (a) and one with an ITO anode of thickness 140 nm (b).

4.3.2 Effect of Film Thickness on Transmittance

The dependence of transmittance on film thickness is investigated experimentally through the preparation of OSC devices with various PEDOT:PSS anode thicknesses. The results of this investigation can be seen in Figure 4.5. At wavelengths below 650 nm, the device with the 75 nm does not follow the expected behaviour, as it exhibits a lower transmittance than the 165 nm and 200 nm devices.

This discrepancy can be explained by an unintentional change in experimental conditions, as the 70 nm and 75 nm devices were prepared on a different day than the 165 nm and 200 nm devices. While an effort was made to keep conditions consistent between the two groups, some conditions like atmospheric pressure are difficult to control without using costly techniques such as vacuum deposition. It can be seen that the 70 nm and 75 nm devices behave nearly identically, with the distance between the two curves nearly constant. Similarly, the 165 nm and 200 nm devices show agreeing behaviour. Hence, the seemingly contradictory behaviour of the 75 nm anode device can be attributed to the unavoidable differences in preparation conditions on two different days in the lab. At wavelengths above 650 nm, the pattern of decreasing transmittance with increasing film thickness is clear, matching the computational results.

4.3.3 Effect of Layer-Layer Interactions

In order to investigate the effects of layer-layer interactions on the optical properties of the devices, transmission spectra were measured after the addition of each layer to the devices. Examples of these spectra are shown in Figures 4.6 and 4.7. In each device,

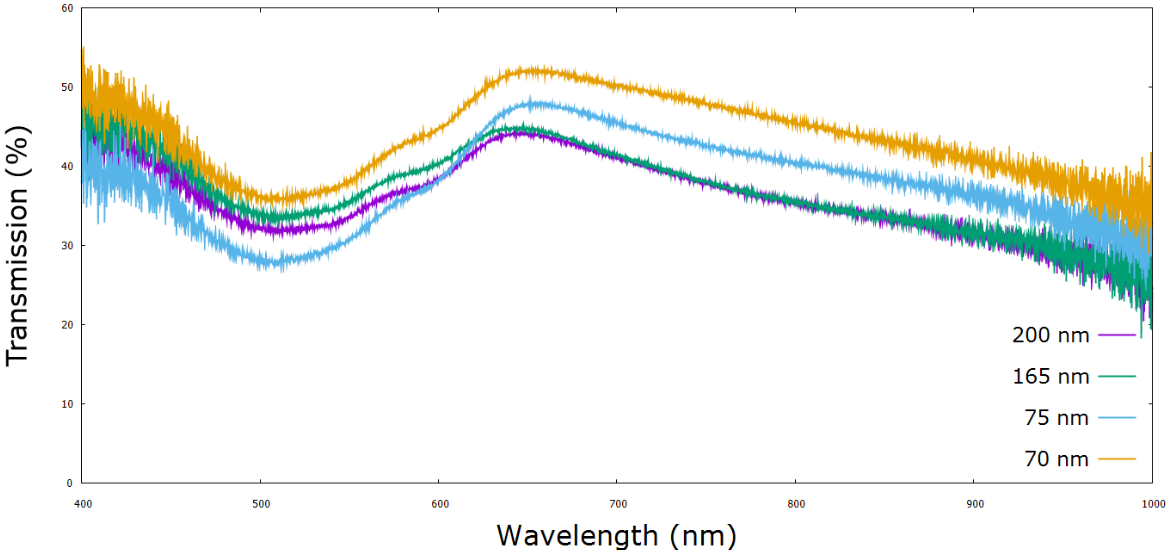

Figure 4.5: Measured transmission spectra of OSC devices with PEDOT:PSS anodes of different thicknesses.

it is clear that the layer with the largest impact on transmission is the P3HT:PCBM active layer. This is how the devices are expected to work, since it is only in the active layer that absorbed light is used to generate electricity. We therefore want to maximize absorption in the active layer, and minimize it in all of the other layers. The transmission spectrum of a single 190 nm layer of P3HT:PCBM on glass is shown in Figure 4.8, showing the low transmission (high absorption) between 400 and 600 nm that explains the behaviour seen in Figures 4.6 and 4.7.

Evidently, there is a much larger drop in transmission due to the addition of the active layer in the cell with the ITO anode (Figure 4.6) than in the cell with the PEDOT:PSS anode (Figure 4.7). As discussed above, this drop in transmission is due to absorption of light by the active layer, which we want to maximize. This suggests, then, that ITO interacts with P3HT:PCBM more favourably than PEDOT:PSS does, as it allows the active layer to absorb more of the incident light. Further discussion of the overall optical performance of the two anode materials can be found below.

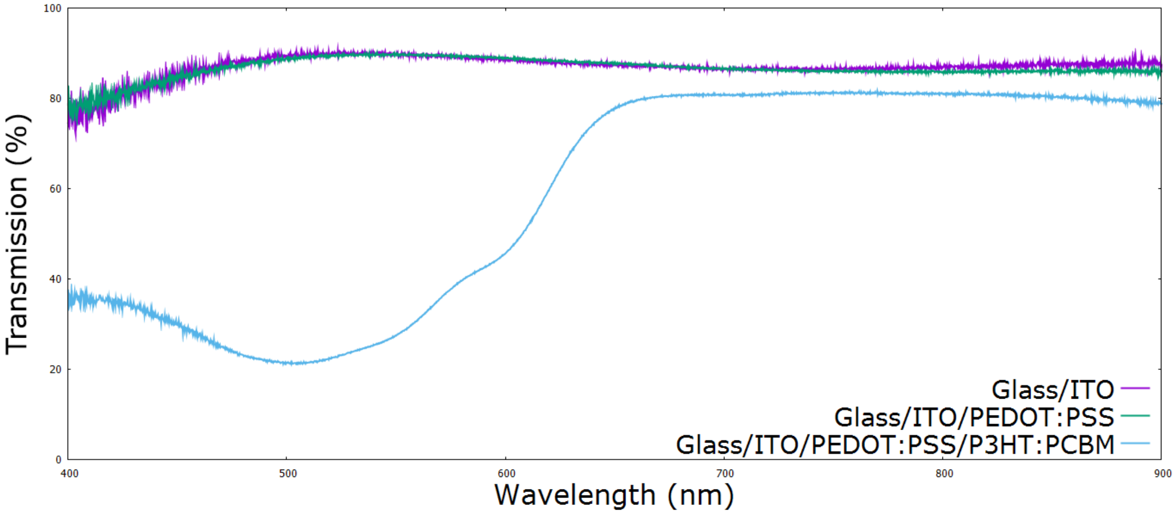

Figure 4.6: Transmission spectra of an OSC device with an ITO anode as each layer of the device is added.

4.3.4 Comparison of ITO and PEDOT:PSS

The optical properties of a device using ITO as the anode material and one using PEDOT:PSS as the anode material are determined experimentally using the methods described in Chapter 3. Five devices with ITO anodes were created under the same conditions, and the average of their transmission spectra was taken. A comparison of the transmission spectra of the devices with ITO anodes versus those with PEDOT:PSS anodes is shown in Figure 4.9.

As was the case with the computational results shown in Figure 4.2, ITO out-

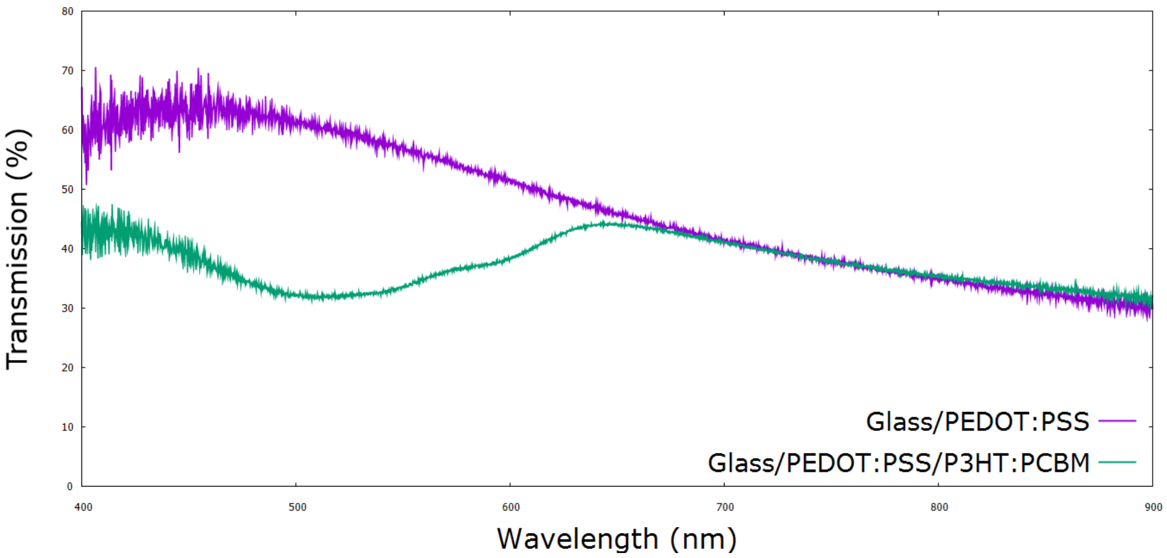

Figure 4.7: Transmission spectra of an OSC device with a PEDOT:PSS anode as each layer of the device is added.

performs PEDOT:PSS at wavelengths greater than 650 nm. In these experimental results, however, the difference between the two was even more pronounced, as the average ITO transmission was 30-45% higher than the various PEDOT:PSS transmissions. At lower wavelengths, between 400-550 nm, the PEDOT:PSS devices outperformed the average ITO device by 8-18%. The ITO and PEDOT:PSS devices have similar transmittances around 625 nm - the peak of the solar spectrum (Figure 3.4) - but the significant increase just past the peak for the devices using ITO makes it the clear choice from an optical perspective. If the PEDOT:PSS anodes are made to be any thinner (less than 70 nm), they would begin to lose their ability to collect holes from the active layer, so this is not a viable strategy for increasing their transmittance. Therefore, in order to be considered a viable alternative anode material, PEDOT:PSS must show significantly better electrical properties than ITO in order

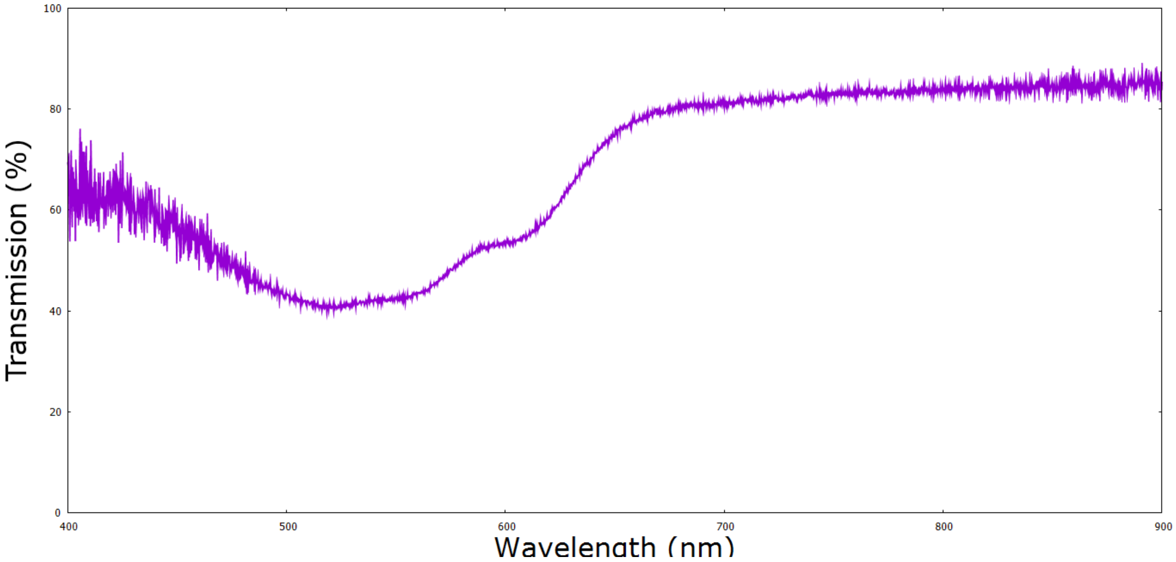

Figure 4.8: Transmission spectrum of a single 190 nm layer of P3HT:PCBM.

to compensate for its clear optical disadvantage.

4.4 Measuring Current-Voltage Properties

In order to fully characterize solar cell performance, a device's electrical properties must be considered in addition to its optical properties. The most common way of assessing a solar cell's electrical performance is by measuring its current-voltage properties, which are summarized in an I-V curve. Using the process described in Section 3.2.3 of this report, the completed devices were characterized electrically under standard solar illumination (Figure 3.4) of 1000 W/m^2.

The results for the devices with ITO anodes are shown in Figure 4.10, while the devices with PEDOT:PSS anodes did not produce measurable I-V curves. All of the devices characterized in Figure 4.10 were prepared under the same conditions, with the same device architectures. In addition to disagreeing with each other, the

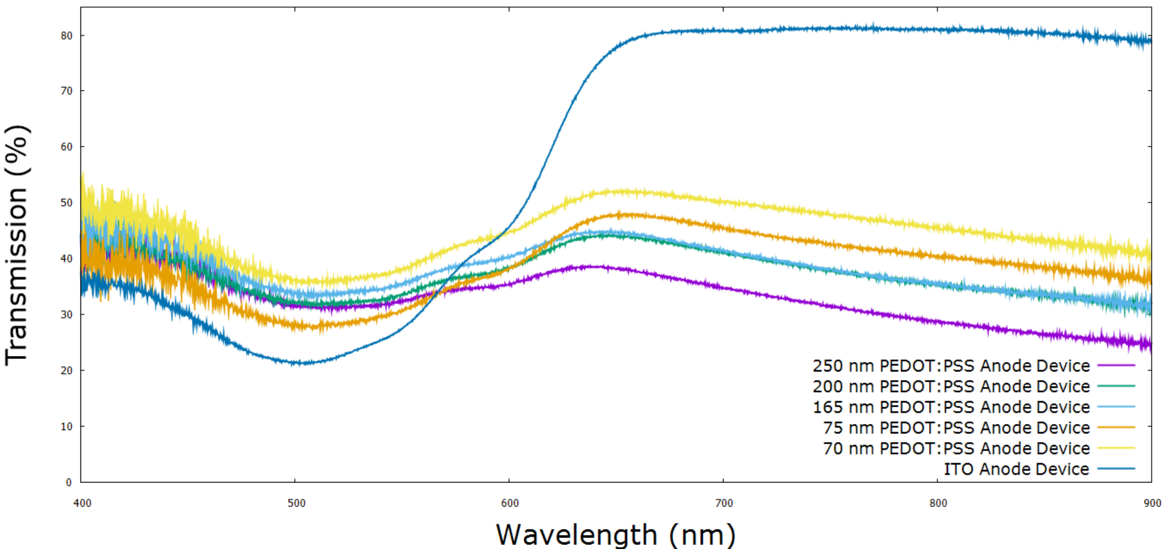

Figure 4.9: Measured transmission spectra of OSC devices with an ITO anode and with PEDOT:PSS anodes of various thicknesses.

current-voltage relationships of these devices is linear, rather than a curve like that shown in Figure 3.5. I suspect that these devices were not electrically complete, since this linear relationship between current and voltage is consistent with Ohm's Law, as one would expect for a resistor, not for a complete solar cell device.

These experiments were attempted for several batches of devices, but all produced similar results. Modifications to the devices were also made in an attempt to boost the devices' I-V performance, such as reducing the size of the silver cathode, but none were successful. This is not expected to be a fault of the measurement technique, since an I-V curve was successfully obtained for a test solar cell, as shown in Figure 3.5. Rather, this behaviour is suspected to be the result of non-uniform morphologies in the prepared thin films allowing current to flow more-or-less unhindered through the devices.

It is reasonable to speculate that a more intricate fabrication process like those in the works of Hunt [21] and Ding [20] could produce OSC devices with reasonable I-V properties, but processes like vacuum deposition and photolithography are beyond the scope of this project, and defeat the purpose of keeping the fabrication process simple and cost-effective.

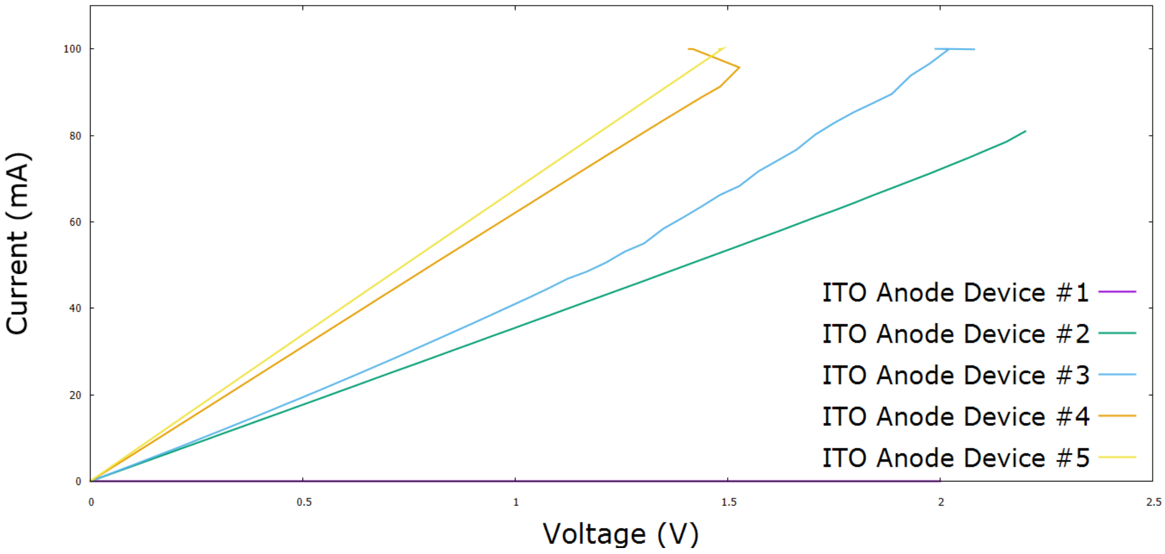

Figure 4.10: Current-Voltage characterization of OSCs with ITO anodes.

Chapter 5

Conclusion

5.1 Summary

The goal of this project was to test the suitability of PEDOT:PSS as an anode material in organic solar cells. Additionally, we sought to optimize the performance of solar cells using PEDOT:PSS as the anode material. The first step in this process was a series of computational trials designed to compare the optical performances of ITO and PEDOT:PSS in OSC architectures. This was followed by a number of experiments that served to confirm the computational results, and to provide insight into the electrical properties of the devices to obtain a more complete comparison.

The computational results indicated that PEDOT:PSS tends to outperform ITO at the lower end of the solar spectrum (between wavelengths of approximately 400 nm - 600 nm) while ITO performs significantly better at the higher end (600 nm and beyond). The experiments confirmed these results, which greatly increased confidence in the model. This trade-off in performance in different regions of the spectrum can be used to ensure that the architectures these materials are used in are optimized from an optical perspective. For example, since PEDOT:PSS shows relatively poor transmission at higher wavelengths, it should be paired with an active layer that absorbs very strongly at low wavelengths, so that the device is not dependent on high-wavelength light being transmitted through the anode layer to perform well.

The compatibility of ITO and PEDOT:PSS with the popular active layer material P3HT:PCBM was then investigated experimentally. By measuring the transmission spectrum of an OSC device before and after application of the active layer, the absorption by the active layer can be inferred by the drop in transmission. It was found that ITO synergized much more effectively with the active layer than PEDOT:PSS did, which makes sense, since ITO and P3HT:PCBM are a standard combination in OSCs, and have thus been engineered to work well together. This test provides a practical metric for how well each material works with existing standards, and once again indicates that ITO outperforms PEDOT:PSS from an optical perspective.

In order to obtain a complete characterization of solar cell performance, electrical properties must be taken into account. Current-Voltage characteristics of OSCs with ITO and PEDOT:PSS anodes were measured, but the results were inconclusive. For the devices with PEDOT:PSS anodes, the I-V curves were all flat, and for thoses with ITO anodes, the current and voltage had a linear relationship, as shown in Figure 4.10. Since we were able to successfully characterize a purchased calibration solar cell, it is not expected that the problem is with the measurement technique, but with the fabrication of the devices. Several batches of devices were prepared and all produced similar results, so it is not expected to be the result of a particular error. Instead, it is concluded that the simplicity of the fabrication process makes it prohibitively difficult to obtain electrically functioning solar cell devices.

To optimize the performance of the PEDOT:PSS anode in each of the tests described above, devices were prepared with various anode thicknesses by varying the spin-coating speed used in the preparation of the PEDOT:PSS films. For the optical tests, the devices with thinner anodes showed higher transmission and therefore better performance, as expected. It is expected that with decreasing thickness, the conductivity of the PEDOT:PSS anode will decrease, thereby balancing the corresponding optical improvement and establishing an interesting trade-off between the two. However, since the electrical tests were inconclusive, the optimization of the PEDOT:PSS anode is also left unresolved.

5.2 Future Work

It would be worthwhile to further examine PEDOT:PSS as a potential anode material, since several parts of this project were inconclusive. If the electrical tests were conducted on samples prepared using a more intricate fabrication process, it may be determined conclusively whether or not PH 510 PEDOT:PSS is suitable as a replacement for ITO in OSCs.

There are also numerous ways one can modify the cells to obtain interesting results. The type of PEDOT:PSS used can be varied, since there are many variations, each with different strengths and weaknesses. Mixing different types of PEDOT:PSS has also been shown to have a large impact on its properties [20], and provides an interesting trade-off that can be optimized for this particular application. The active layer can also be modified to work better with a PEDOT:PSS anode. Using the techniques described in this project, the active layer thickness can easily be modified, simply by modifying the spin-coating speed used in its preparation. This will impact its optical and electrical properties as it did for the PEDOT:PSS, and can therefore be varied to optimize overall solar cell performance.

An interesting challenge facing the adoption of OSCs into practical applications is their stability in ambient conditions. In the presence of water, device performance decays rapidly, as the organic components of the solar cells are very hydrophilic [28]. Unless the devices are completely enclosed, their performance will quickly and irreversibly decline due to the absorption of moisture from the air. However, enclosing the cells limits the amount of light reaching the devices due to the absorption and reflection of the enclosing material. Recently, a photolithographic technique was shown to increase the long-term stability of PEDOT:PSS while maintaining its high conductivity [29]. This technique was used to fabricate stable organic humidity sensors, but might be applicable to OSCs as well. An investigation of how this process effects not only the stability of the cells, but also their optical and electrical performance may prove very interesting.

A relatively new class of solar cells called perovskites would also be very valuable to investigate. These materials combine the simple and cost-effective fabrication process of OSCs with the high efficiency of traditional silicon-based devices [30]. Perovskite solar cell architectures often include PEDOT:PSS as a hole-conducting buffer layer. The techniques for modifying the PEDOT:PSS anode layer discussed throughout this report can be attempted on this buffer layer, since modifying the optical and electrical properties of the buffer layer should have a significant impact on device performance. Additionally, perovskites suffer from the same stability issues as organics, so applying the photolithographic technique mentioned above to the PEDOT:PSS buffer layer could significantly improve device stability.

Bibliography

[1] Jenny Nelson. *The Physics of Solar Cells*. Imperial College Press, 2003.

[2] Hui Huang. *Organic and Hybrid Solar Cells*. Springer, 2014.

[3] National Renewable Energy Laboratories. *Best Research-Cell Efficiency Chart*. URL: `https://www.nrel.gov/pv/cell-efficiency.html`.

[4] Wolfgang Tress. *Organic Solar Cells: Theory, Experiment, and Device Simulation*. Springer, 2014.

[5] Omar Abdulrazzaq, Viney Saini, Shawn Bourdo, Enkeleda Dervishi, and Alexandru Biris. "Organic Solar Cells: A Review of Materials, Limitations, and Possibilities for Improvement". *Particulate Science and Technology* 31 (2013), pp. 427–442.

[6] T. Lei, R. Peng, W. Song, L. Hong, J. Huang, N. Feia, and Z. Ge. "Bendable and foldable flexible organic solar cells based on Ag nanowire films with 10.30% efficiency". *Journal of Materials Chemistry A* 7 (2019), pp. 3737–3744.

[7] A. Husaina, W. Hasana, S. Shafie, M. Hamidon, and S. Pandey. "A review of transparent solar photovoltaic technologies". *Renewable and Sustainable Energy Reviews* 94 (2018), pp. 779–791.

[8] Wallace Choy. *Organic Solar Cells: Materials and Device Physics*. Springer, 2013.

[9] Hooman Mehdizadeh Rad, Furong Zhu, and Jai Singh. "Profiling exciton generation and recombination in conventional and inverted bulk heterojunction organic solar cells". *IOSR Journal of Applied Physics* 124.8 (2018), p. 124.

[10] Nevena Marinova, Silvia Valero, and Juan Luis Delgado. "Organic and Perovskite Solar Cells: Working Principles, Materials and Interfaces". *Journal of Colloid and Interface Science* 488 (2017), pp. 373–389.

[11] S. Matthew Menke, Niva A. Ran, Guillermo C. Bazan, and Richard H. Friend. "Understanding Energy Loss in Organic Solar Cells: Toward a New Efficiency Regime". *Joule* 2 (2018), pp. 25–35.

[12] Wolfgang Brütting. *Physics of Organic Semiconductors*. Wiley-VCH, 2005.

[13] Seok-In Na, Seok-Soon Kim, Jang Jo, and Dong-Yu Kim. "Efficient and Flexible ITO-Free Organic Solar Cells Using Highly Conductive Polymer Anodes". *Advanced Materials* 20.21 (2008), pp. 4061–4067.

[14] O. Yu. Posudievskya, N.V. Konoshchuka, A.G. Shkavro, V.G. Koshechkoa, and V.D. Pokhodenkoa. "Structure and electronic properties of poly (3,4 - ethylenedioxythiophene) poly(styrene sulfonate) prepared under ultrasonic irradiation". *Synthetic Metals* 195 (2014), pp. 335–339.

[15] H. Bednarski, B. Hajduk, J. Jurusik, B. Jarzabek, M. Domanski, K. Laba, A. Wanic, and M. Lapkowski. "The Influence of PEDOT to PSS Ratio on the Optical Properties of PEDOT:PSS Thin Solid Films — Insight from Spectroscopic Ellipsometry". *Acta Physica Polonica A* 130.5 (2016), pp. 1242–1244.

[16] Heraeus Inc. *Clevios PH 510 PEDOT:PSS Data Sheet.* URL: `http://www.lookpolymers.com/pdf/Heraeus-Clevios-PH-510-Conductive-Sulfonate-Polymer-for-Antistatic-Coatings.pdf`.

[17] Steven J. Byrnes. “Multilayer Optical Calculations”. *Cornell University arXiv* 1603.02720 (2016).

[18] George F. Burkhard, Eric T. Hoke, and Michael D. McGehee. “Accounting for Interference, Scattering, and Electrode Absorption to Make Accurate Internal Quantum Efficiency Measurements in Organic and Other Thin Solar Cells”. *Advanced Materials* 22.30 (2010), pp. 3293–3297.

[19] Frank L. Pedrotti, Leno M. Pedrotti, Leno S. Pedrotti. *Introduction to Optics, 2nd Ed.* Prentice-Hall, 1993.

[20] Yanfei Ding. “*Organic bulk heterojunction solar cells with improved efficiency*”. MA thesis. Memorial University of Newfoundland, 2009.

[21] Matthew Hunt. “*Improving the efficiency of organic solar cells through the addition of silver nanoparticles and cadmium oxide*”. MA thesis. Memorial University of Newfoundland, 2016.

[22] Delta Technologies, Ltd. *Corning Boro-Aluminosilicate Glass Products.* URL: `http://www.delta-technologies.com/products.asp?C=1`.

[23] Heraeus Inc. *Clevios P VP Al 4083 PEDOT:PSS Data Sheet.* URL: `https://www.heraeus.com/media/media/hec/documents_hec/data_sheets_hep/Clevios_P_VP_AI_4083.pdf`.

[24] Z. Su, L. Wang, Y. Li, H. Zhao, B. Chu, and W. Li. “Ultraviolet-ozone-treated PEDOT:PSS as anode buffer layer for organic solar cells”. *Nanoscale Research Letters* 7 (2012), p. 465.

[25] National Renewable Energy Laboratories. *Reference Air Mass 1.5 Spectra.* URL: `https://www.nrel.gov/grid/solar-resource/spectra-am1.5.html`.

[26] Dechan Angmo and Frederik C. Krebs. “Flexible ITO-free polymer solar cells”. *Journal of Applied Polymer Science* (2012).

[27] Ossila, Inc. *Spin Coating: A Guide to Theory and Techniques.* URL: `https://www.ossila.com/pages/spin-coating`.

[28] Pei Cheng and Xiaowei Zhan. “Stability of organic solar cells: challenges and strategies”. *Chemical Society Reviews* 45 (2016), pp. 2544–2582.

[29] Zijie Zhu, Gaomai Yang, Ruya Li, Tingrui Pan. “Photopatternable PEDOT:PSS / PEG hybrid thin film with moisture stability and sensitivity”. *Microsystems and Nanoengineering* 3 (2017).

[30] Ajay Kumar Jena, Ashish Kulkarni, and Tsutomu Miyasaka. “Halide Perovskite Photovoltaics: Background, Status, and Future Prospects”. *Chemical Reviews* 119.5 (2019), pp. 3036–3103.

Appendix A

Appendix – Modelling Implementation

Below is the code used to implement the optical model described in Chapter 2 of this report. It was written in Python 3, using Jupyter Notebook to edit, compile and run the code.

Buffer Layer Optimization

By: John Healey

Introduction

We are studying the effect of using different kinds of PEDOT in the PEDOT:PSS buffer layer on the device's photon absorption and internal optical electrical field distribution. We will also determine the ITO thickness that optimizes these parameters.

We will be using Transfer Matrix Formalism (TMF) to evaluate these properties, which is explained here (https://aip.scitation.org/doi/abs/10.1063/1.370757), and summarized below.

Theory behind TMF

Interface Matrices

Each interface in the structure (between layers j and k) can be described by an interface matrix of the form:

$$I_{jk} = \frac{1}{t_{jk}} \begin{bmatrix} 1 & r_{jk} \\ r_{jk} & 1 \end{bmatrix}$$

where r_{jk} and t_{jk} are the Fresnel complex *reflection* and *transmission* coefficients at interface jk.

These coefficients are given by:

$$r_{jk} = \frac{q_j - q_k}{q_j + q_k},$$

$$t_{jk} = \frac{2q_j}{q_j + q_k}$$

where

$$q_j = [\tilde{n}_j^2 - \eta_0^2 sin\phi_0]^{\frac{1}{2}}$$

We assume that ϕ_0 is 0, so q_j is simplified to $\tilde{n}_j$ - the complex index of refraction of layer j, which is determined experimentally:

$$q_j = \tilde{n}_j = \eta_j + ik_j,$$

where η_j and k_j are the refractive index and extinction coefficient of layer j.

Layer Matrices

The layer matrix describing the propagation through layer j is given by:

$$L_j = \begin{bmatrix} e^{-i\xi_j d_j} & 0 \\ 0 & e^{i\xi_j d_j} \end{bmatrix}$$

where

$$\xi_j = \frac{2\pi}{\lambda} q_j$$

and $\xi_j d_j$ is the *layer phase thickness*, corresponding to the phase change the wave experiences as it traverses layer j.

System Transfer Matrix

By using the interface and layer matrices, the total system transfer matrix (scattering matrix) S can be written:

$$S = \begin{bmatrix} S_{11} & S_{12} \\ S_{21} & S_{22} \end{bmatrix} = (\prod_{v=1}^{m} I_{(v-1)v} L_v) I_{m(m+1)}$$

This matrix relates the electric field at the ambient side and susbstrate side (Aluminum cathode - layer m+1) by:

$$\begin{bmatrix} E_0^+ \\ E_0^- \end{bmatrix} = S \begin{bmatrix} E_{m+1}^+ \\ E_{m+1}^- \end{bmatrix}$$

where the optical electric field at any point in the system is resolved into two components: one component propagating in the positive x direction and one in the negative x direction, which at a position x in layer j are denoted $E_j^+(x)$ and $E_j^-(x)$

For the total layered structure, the resulting complex reflection and transmission coefficients can be expressed by using the matrix elements of the total system transfer matrix:

$$r = \frac{E_0^-}{E_0^+} = \frac{S_{21}}{S_{11}},$$

$$t = \frac{E_{m+1}^+}{E_0^+} = \frac{1}{S_{11}}.$$

Calculating Internal Electric Field

In order to calculate the internal electric field in layer j, the layers can be divided into two subsets: one subset to the left of j which will be represented by S'_j, and one subset to the right of j which we'll represent with S''_j.

The total system transfer matrix can then be written as

$$S = S'_j L_j S''_j$$

The partial system transfer matrix for the layers left of j is equal to

$$S'_j = \begin{bmatrix} S'_{j11} & S'_{j12} \\ S'_{j21} & S'_{j22} \end{bmatrix} = (\prod_{v=1}^{j-1} I_{(v-1)v} L_v) I_{(j-1)j}.$$

For the layers right of j, the matrix is

$$S''_j = \begin{bmatrix} S''_{j11} & S''_{j12} \\ S''_{j21} & S''_{j22} \end{bmatrix} = (\prod_{v=j+1}^{m} I_{(v-1)v} L_v) I_{m(m+1)}.$$

The expression for the total electric field at distance x from the left boundary of layer j is:

$$E_j(x) = \frac{S''_{j11} \cdot e^{-i\xi_j (d_j - x)} + S''_{j21} \cdot e^{i\xi_j (d_j - x)}}{S'_{j11} S''_{j11} \cdot e^{-i\xi_j d_j} + S'_{j12} S''_{j21} \cdot e^{i\xi_j d_j}} E_0^+,$$

where $0 \leq x \leq d$.

Calculation

Setting up constants

In [1]:

```
import numpy as np
from matplotlib import pyplot as plt
import math
import cmath
import copy

wavelength = 632.8 # nm
m = 3 # no. of layers between ambient and substrate
```

Interface Matrices

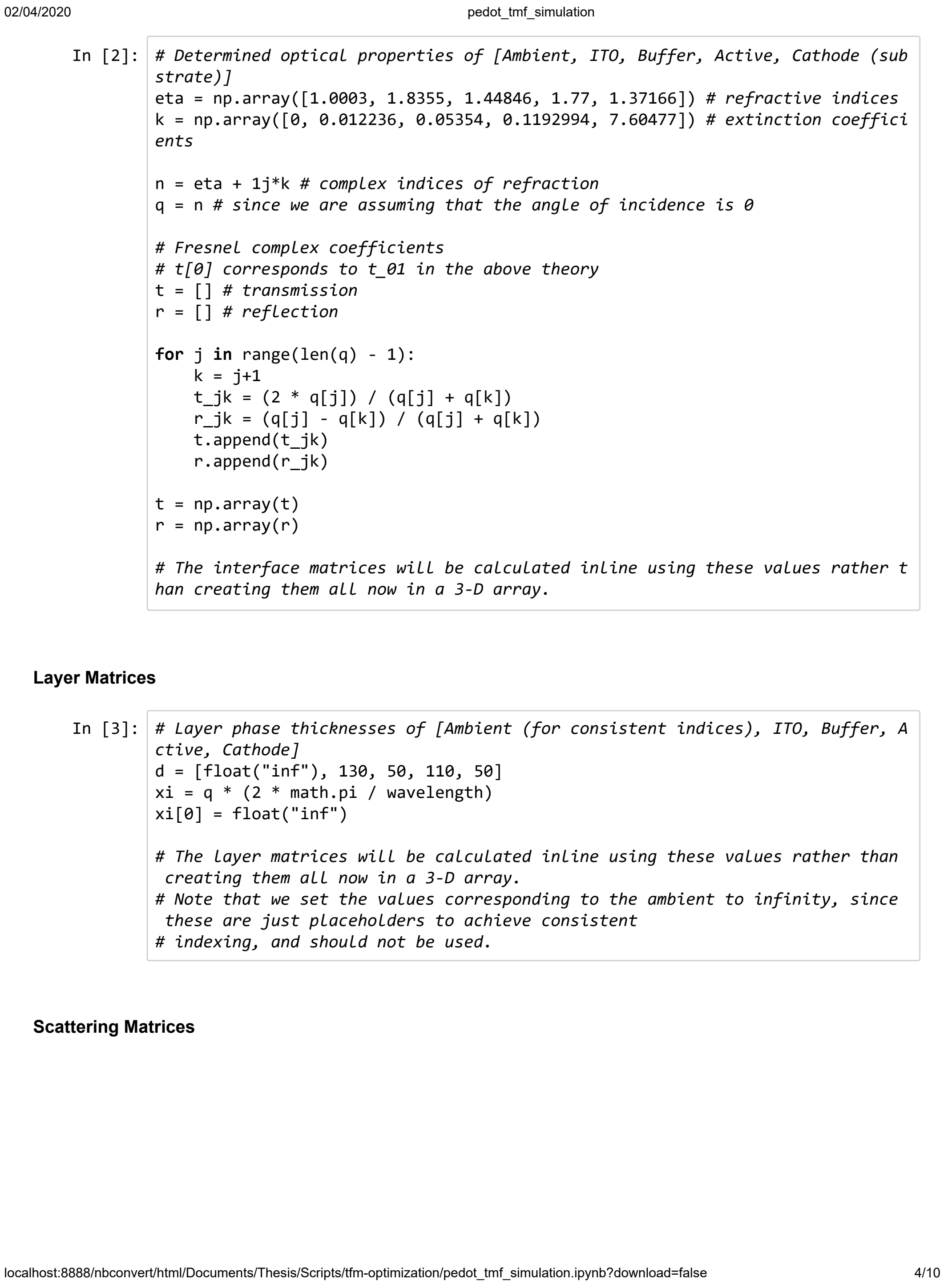

In [2]:

```
# Determined optical properties of [Ambient, ITO, Buffer, Active, Cathode (sub
strate)]
eta = np.array([1.0003, 1.8355, 1.44846, 1.77, 1.37166]) # refractive indices
k = np.array([0, 0.012236, 0.05354, 0.1192994, 7.60477]) # extinction coeffici
ents

n = eta + 1j*k # complex indices of refraction
q = n # since we are assuming that the angle of incidence is 0

# Fresnel complex coefficients
# t[0] corresponds to t_01 in the above theory
t = [] # transmission
r = [] # reflection

for j in range(len(q) - 1):
    k = j+1
    t_jk = (2 * q[j]) / (q[j] + q[k])
    r_jk = (q[j] - q[k]) / (q[j] + q[k])
    t.append(t_jk)
    r.append(r_jk)

t = np.array(t)
r = np.array(r)

# The interface matrices will be calculated inline using these values rather t
han creating them all now in a 3-D array.
```

Layer Matrices

In [3]:

```
# Layer phase thicknesses of [Ambient (for consistent indices), ITO, Buffer, A
ctive, Cathode]
d = [float("inf"), 130, 50, 110, 50]
xi = q * (2 * math.pi / wavelength)
xi[0] = float("inf")

# The layer matrices will be calculated inline using these values rather than
 creating them all now in a 3-D array.
# Note that we set the values corresponding to the ambient to infinity, since
 these are just placeholders to achieve consistent
# indexing, and should not be used.
```

Scattering Matrices

In [4]:

```
# Returns the scattering matrix corresponding to the given layers
def scattering_matrix(start_layer, stop_layer, trans, refl, thick, phase):
    prod = np.identity(2) # initial value of cumulative product
    for v in range(start_layer, stop_layer+1):
        # interface matrix I_(v-1)v
        t_jk = trans[v-1]
        r_jk = refl[v-1]
        I_v = (1 / t_jk) * np.array([
                                        [1, r_jk],
                                        [r_jk, 1]
                                    ])

        # layer matrix L_v
        phase_thickness = phase[v] * thick[v]
        L_v = np.array([
                            [cmath.exp(-1j*phase_thickness), 0],
                            [0, cmath.exp(1j*phase_thickness)]
                       ])

        inner_prod = np.matmul(I_v, L_v)

        prod = np.matmul(prod, inner_prod) # update cumulative product

    outer_interface = (1 / trans[stop_layer]) * np.array([
                                                            [1, refl[stop_laye
r]],
                                                            [refl[stop_layer],
1]
                                                         ])
    return np.matmul(prod, outer_interface)
```

Optimizing the internal optical electric field

Here, we calculate the distribution of the normalized modulus squared of the incident optical electric field of the device using two different buffer layers.

In [5]:

```
# Returns the electric field at point x in layer j, given the partial scatteri
ng matrices.
def electric_field(S_left, S_right, j, x, thick, phase):
    exp_1 = cmath.exp(-1j*phase[j] * (thick[j]-x))
    exp_2 = cmath.exp(1j*phase[j] * (thick[j]-x))
    numerator = (S_right[0][0] * exp_1) + (S_right[1][0] * exp_2)

    exp_3 = cmath.exp(-1j*phase[j]*thick[j])
    exp_4 = cmath.exp(1j*phase[j]*thick[j])
    denominator = (S_left[0][0] * S_right[0][0] * exp_3) + (S_left[0][1] * S_r
ight[1][0] * exp_4)

    return numerator/denominator
```

Modified buffer layer parameters

In [6]:

```
# Determined optical properties of [Ambient, ITO, Modified Buffer, Active, Cat
hode (substrate)]
eta_mod = np.array([1.0003, 1.8355, 1.34846, 1.77, 1.37166]) # refractive indi
ces
k_mod = np.array([0, 0.012236, 0.05354, 0.1192994, 7.60477]) # extinction coef
ficients
n_mod = eta_mod + 1j*k_mod # complex indices of refraction
q_mod = n_mod # since we are assuming that the angle of incidence is 0

# Fresnel complex coefficients
# t[0] corresponds to t_01 in the above theory
t_mod = [] # transmission
r_mod = [] # reflection

for j in range(len(q_mod) - 1):
    k = j+1
    t_jk = (2 * q_mod[j]) / (q_mod[j] + q_mod[k])
    r_jk = (q_mod[j] - q_mod[k]) / (q_mod[j] + q_mod[k])
    t_mod.append(t_jk)
    r_mod.append(r_jk)

t_mod = np.array(t_mod)
r_mod = np.array(r_mod)
xi_mod = q_mod * (2 * math.pi / wavelength)
xi_mod[0] = float("inf")
```

Electric field comparison

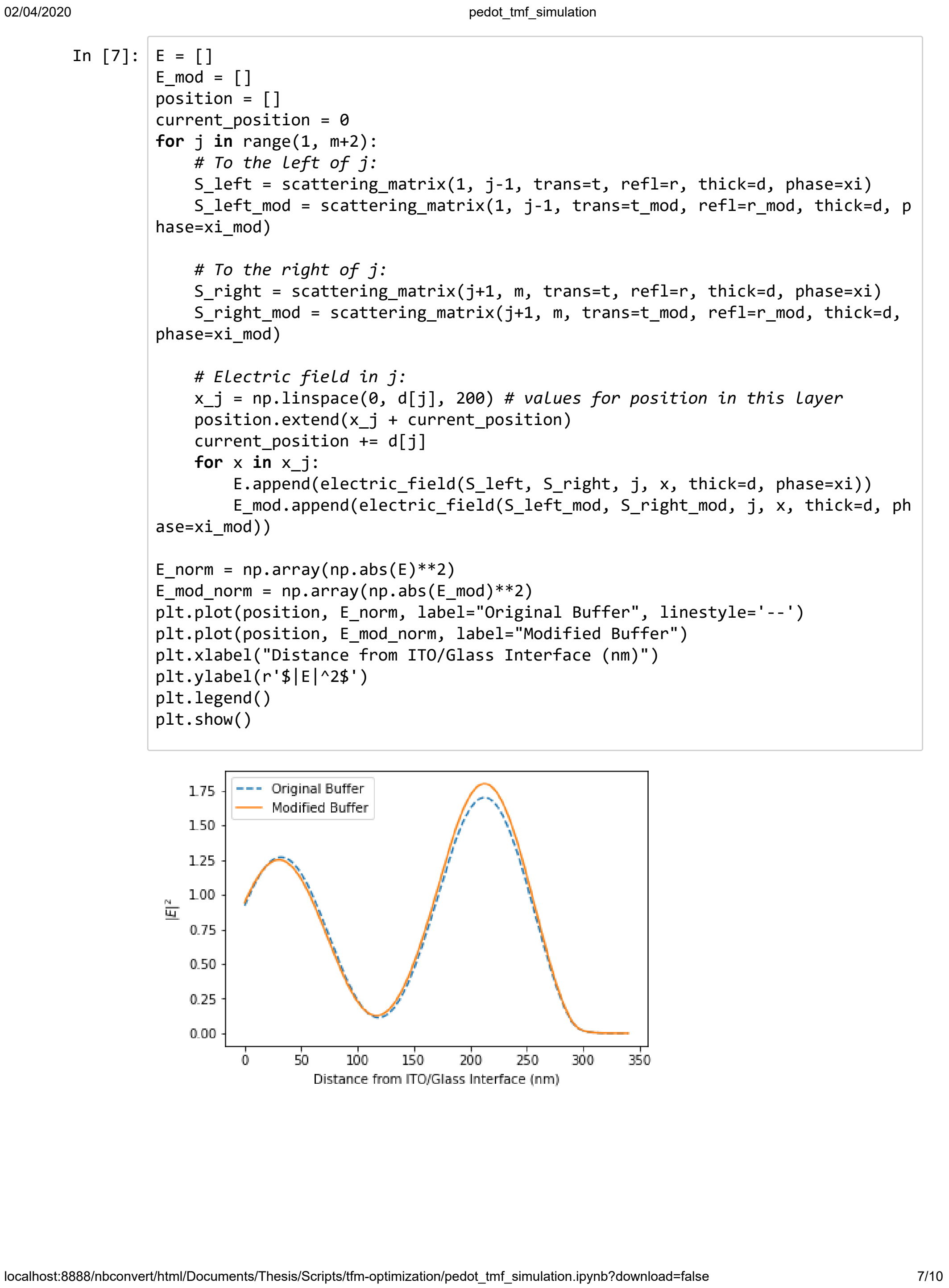

02/04/2020 pedot_tmf_simulation

In [7]:

```
E = []
E_mod = []
position = []
current_position = 0
for j in range(1, m+2):
    # To the left of j:
    S_left = scattering_matrix(1, j-1, trans=t, refl=r, thick=d, phase=xi)
    S_left_mod = scattering_matrix(1, j-1, trans=t_mod, refl=r_mod, thick=d, p
hase=xi_mod)

    # To the right of j:
    S_right = scattering_matrix(j+1, m, trans=t, refl=r, thick=d, phase=xi)
    S_right_mod = scattering_matrix(j+1, m, trans=t_mod, refl=r_mod, thick=d,
phase=xi_mod)

    # Electric field in j:
    x_j = np.linspace(0, d[j], 200) # values for position in this layer
    position.extend(x_j + current_position)
    current_position += d[j]
    for x in x_j:
        E.append(electric_field(S_left, S_right, j, x, thick=d, phase=xi))
        E_mod.append(electric_field(S_left_mod, S_right_mod, j, x, thick=d, ph
ase=xi_mod))

E_norm = np.array(np.abs(E)**2)
E_mod_norm = np.array(np.abs(E_mod)**2)
plt.plot(position, E_norm, label="Original Buffer", linestyle='--')
plt.plot(position, E_mod_norm, label="Modified Buffer")
plt.xlabel("Distance from ITO/Glass Interface (nm)")
plt.ylabel(r'$|E|^2$')
plt.legend()
plt.show()
```

localhost:8888/nbconvert/html/Documents/Thesis/Scripts/tfm-optimization/pedot_tmf_simulation.ipynb?download=false 7/10

Further optimizing the internal optical electric field

Here, we once again calculate the normalized modulus squared of the incident optical electric field of the device, this time using ITO of various thicknesses.

In [8]:

```
d_mod = [-1, 100, 50, 110, 50]
E_ito_mod = []
position_ito_mod = []
current_position = 0
for j in range(1, m+2):
    # To the left of j:
    S_left = scattering_matrix(1, j-1, trans=t, refl=r, thick=d_mod, phase=xi)

    # To the right of j:
    S_right = scattering_matrix(j+1, m, trans=t, refl=r, thick=d_mod, phase=xi
)

    # Electric field in j:
    x_j = np.linspace(0, d_mod[j], 200) # values for position in this layer
    position_ito_mod.extend(x_j + current_position)
    current_position += d_mod[j]
    for x in x_j:
        E_ito_mod.append(electric_field(S_left, S_right, j, x, thick=d_mod, ph
ase=xi))

E_ito_mod_norm = np.array(np.abs(E_ito_mod)**2)
plt.plot(position, E_norm, label="Original Architecture", linestyle='--')
plt.plot(position, E_mod_norm, label="Modified Buffer")
plt.plot(position_ito_mod, E_ito_mod_norm, label="Modified ITO")
plt.xlabel("Distance from ITO/Glass Interface (nm)")
plt.ylabel(r'$|E|^2$')
plt.legend()
plt.show()
```

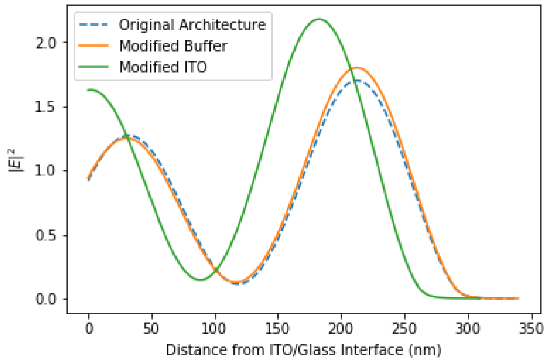

Optimizing photon absorption

Here, we calculate the absorption and reflectance of the device using various ITO thicknesses.

In [9]:
```
ito_thicknesses = np.arange(10, 180, 10) # thicknesses of ITO layer to be test
ed
layer_thicknesses = copy.copy(d) # shallow copy so we don't change d
R = []
A = []
for d_ito in ito_thicknesses:
    layer_thicknesses[1] = d_ito
    S = scattering_matrix(start_layer=1, stop_layer=m, trans=t, refl=r, thick=
layer_thicknesses, phase=xi)
    r_complex = S[1][0] / S[0][0]
    reflectivity = np.abs(r_complex)**2
    R.append(reflectivity)
    A.append(1 - reflectivity)
plt.scatter(ito_thicknesses, R, s=5)
plt.xlabel("ITO thickness (nm)")
plt.ylabel("Reflectivity at 632.8 nm")
plt.show()
```

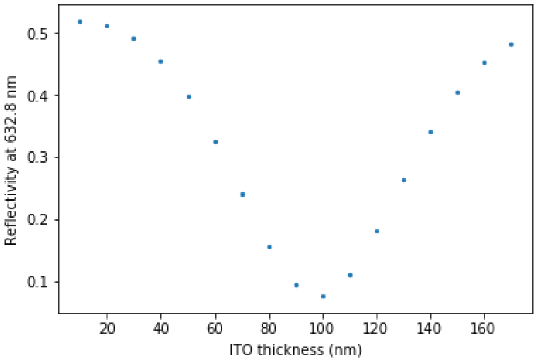

In [10]:

```
plt.scatter(ito_thicknesses, A, s=5)
plt.xlabel("ITO thickness (nm)")
plt.ylabel("Absorption at 632.8 nm")
plt.show()
```

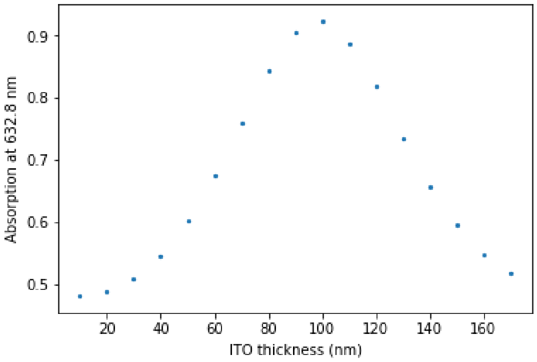

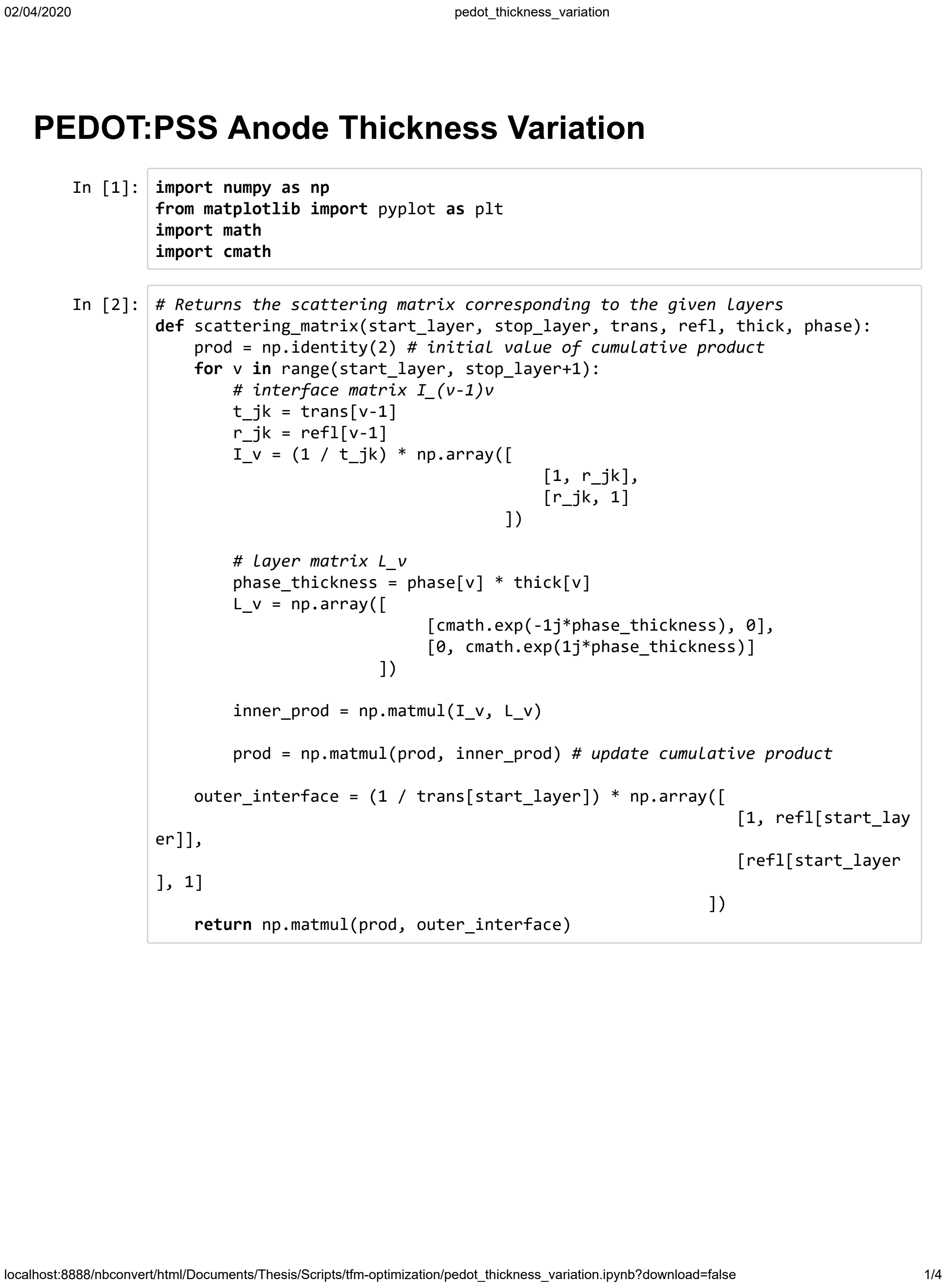

PEDOT:PSS Anode Thickness Variation

In [1]:

```
import numpy as np
from matplotlib import pyplot as plt
import math
import cmath
```

In [2]:

```
# Returns the scattering matrix corresponding to the given layers
def scattering_matrix(start_layer, stop_layer, trans, refl, thick, phase):
    prod = np.identity(2) # initial value of cumulative product
    for v in range(start_layer, stop_layer+1):
        # interface matrix I_(v-1)v
        t_jk = trans[v-1]
        r_jk = refl[v-1]
        I_v = (1 / t_jk) * np.array([
                                        [1, r_jk],
                                        [r_jk, 1]
                                    ])

        # layer matrix L_v
        phase_thickness = phase[v] * thick[v]
        L_v = np.array([
                            [cmath.exp(-1j*phase_thickness), 0],
                            [0, cmath.exp(1j*phase_thickness)]
                        ])

        inner_prod = np.matmul(I_v, L_v)

        prod = np.matmul(prod, inner_prod) # update cumulative product

    outer_interface = (1 / trans[start_layer]) * np.array([
                                                            [1, refl[start_lay
er]],
                                                            [refl[start_layer
], 1]
                                                        ])
    return np.matmul(prod, outer_interface)
```

```
In [3]: pedot_anode_eta = []
        pedot_anode_k = []
        pedot_anode_wavelengths = []
        for line in open('data/nk_PEDOT.csv'):
            row = line.strip().split(',')
            if row[0].isdigit():
                pedot_anode_wavelengths.append(int(row[0]))
                pedot_anode_eta.append(float(row[1]))
                pedot_anode_k.append(float(row[2]))
        pedot_anode_n = np.array(pedot_anode_eta) + 1j*np.array(pedot_anode_k) # compl
        ex indices of refraction
        pedot_anode_q = pedot_anode_n # since we are assuming that the angle of incide
        nce is 0
        pedot_anode_q = dict(zip(pedot_anode_wavelengths, pedot_anode_q))
```

```
In [4]: p3ht_eta = []
        p3ht_k = []
        p3ht_wavelengths = []
        for line in open('data/nk_P3HTPCBM_BHJ.csv'):
            row = line.strip().split(',')
            if row[0].isdigit():
                p3ht_wavelengths.append(int(row[0]))
                p3ht_eta.append(float(row[1]))
                p3ht_k.append(float(row[2]))
        p3ht_n = np.array(p3ht_eta) + 1j*np.array(p3ht_k) # complex indices of refract
        ion
        p3ht_q = np.array(p3ht_n) # since we are assuming that the angle of incidence
         is 0
        p3ht_q = dict(zip(p3ht_wavelengths, p3ht_q))
```

```
In [5]: ambient_eta = np.ones(len(pedot_anode_wavelengths))*0.13
        ambient_k = np.ones(len(pedot_anode_wavelengths))*2.92
        ambient_n = np.array(ambient_eta) + 1j*np.array(ambient_k) # complex indices o
        f refraction
        ambient_q = np.array(ambient_n) # since we are assuming that the angle of inci
        dence is 0
        ambient_q = dict(zip(pedot_anode_wavelengths, ambient_q))

        pedot_device_q = [ambient_q, pedot_anode_q, p3ht_q, ambient_q]
```

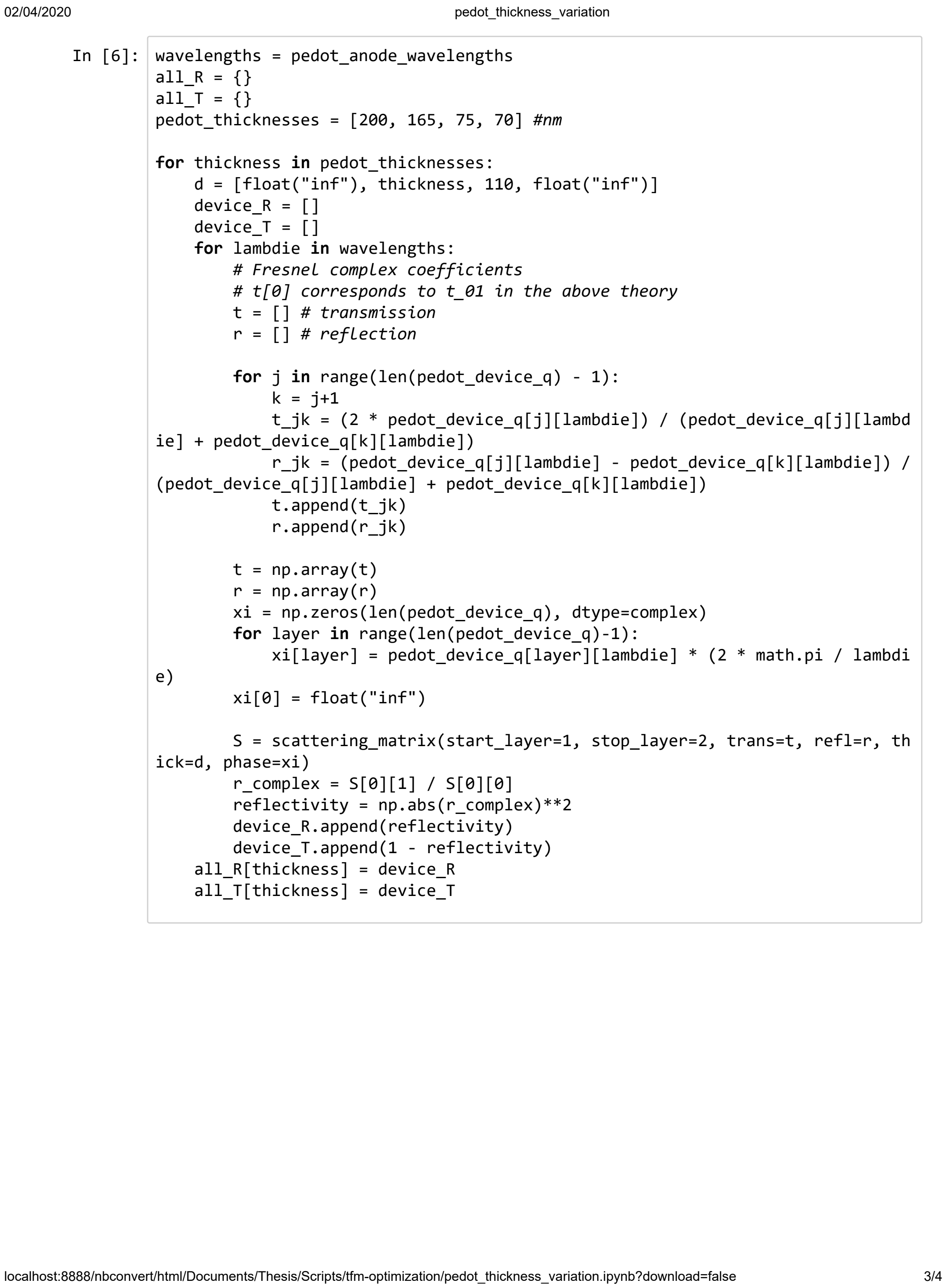

02/04/2020 pedot_thickness_variation

```
In [6]: wavelengths = pedot_anode_wavelengths
        all_R = {}
        all_T = {}
        pedot_thicknesses = [200, 165, 75, 70] #nm

        for thickness in pedot_thicknesses:
            d = [float("inf"), thickness, 110, float("inf")]
            device_R = []
            device_T = []
            for lambdie in wavelengths:
                # Fresnel complex coefficients
                # t[0] corresponds to t_01 in the above theory
                t = [] # transmission
                r = [] # reflection

                for j in range(len(pedot_device_q) - 1):
                    k = j+1
                    t_jk = (2 * pedot_device_q[j][lambdie]) / (pedot_device_q[j][lambd
        ie] + pedot_device_q[k][lambdie])
                    r_jk = (pedot_device_q[j][lambdie] - pedot_device_q[k][lambdie]) /
        (pedot_device_q[j][lambdie] + pedot_device_q[k][lambdie])
                    t.append(t_jk)
                    r.append(r_jk)

                t = np.array(t)
                r = np.array(r)
                xi = np.zeros(len(pedot_device_q), dtype=complex)
                for layer in range(len(pedot_device_q)-1):
                    xi[layer] = pedot_device_q[layer][lambdie] * (2 * math.pi / lambdi
        e)
                xi[0] = float("inf")

                S = scattering_matrix(start_layer=1, stop_layer=2, trans=t, refl=r, th
        ick=d, phase=xi)
                r_complex = S[0][1] / S[0][0]
                reflectivity = np.abs(r_complex)**2
                device_R.append(reflectivity)
                device_T.append(1 - reflectivity)
            all_R[thickness] = device_R
            all_T[thickness] = device_T
```

localhost:8888/nbconvert/html/Documents/Thesis/Scripts/tfm-optimization/pedot_thickness_variation.ipynb?download=false 3/4

In [7]:

```
for thickness in pedot_thicknesses:
    plt.plot(wavelengths[100:], np.ones(len(all_T[thickness][100:]))-all_T[thickness][100:], label=str(thickness)+' nm')
plt.xlabel("Wavelength (nm)")
plt.ylabel("Transmission")
plt.ylim(0, 0.8)
plt.xlim(300, 850)
plt.legend()
plt.show()
```

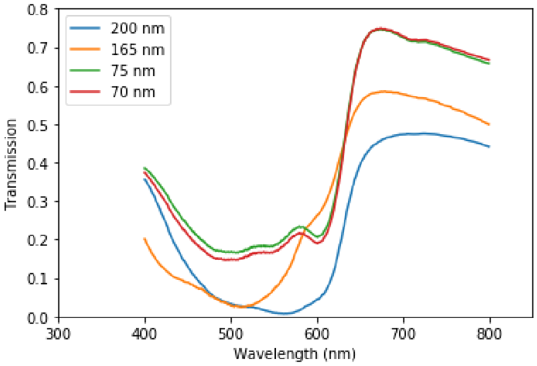

Write each transmission to file

In [16]:

```
for thickness in pedot_thicknesses:
    pedot_file = open(f'Predicted_PEDOT_%dnm.dat' % (thickness), 'w')
    for i in range(len(wavelengths[100:])):
        pedot_file.write(f'{wavelengths[100:][i]}\t{(1-all_T[thickness][100:][i])*100}\n')
    pedot_file.close()
```

ITO Anode

In [1]:

```
import numpy as np
from matplotlib import pyplot as plt
import math
import cmath
```

In [2]:

```
d = [float("inf"), 130, 50, 110, float("inf")]

ito_eta = []
ito_k = []
ito_wavelengths = []
for line in open('data/nk_ITO.csv'):
    row = line.strip().split(',')
    if row[0].isdigit():
        ito_wavelengths.append(int(row[0]))
        ito_eta.append(float(row[1]))
        ito_k.append(float(row[2]))
ito_n = np.array(ito_eta) + 1j*np.array(ito_k) # complex indices of refraction
ito_q = ito_n # since we are assuming that the angle of incidence is 0
ito_q = dict(zip(ito_wavelengths, ito_q))
```

In [3]:

```
pedot_eta = []
pedot_k = []
pedot_wavelengths = []
for line in open('data/nk_PEDOT.csv'):
    row = line.strip().split(',')
    if row[0].isdigit():
        pedot_wavelengths.append(int(row[0]))
        pedot_eta.append(float(row[1]))
        pedot_k.append(float(row[2]))
pedot_n = np.array(pedot_eta) + 1j*np.array(pedot_k) # complex indices of refr
action
pedot_q = pedot_n # since we are assuming that the angle of incidence is 0
pedot_q = dict(zip(pedot_wavelengths, pedot_q))
```

In [4]:

```
p3ht_eta = []
p3ht_k = []
p3ht_wavelengths = []
for line in open('data/nk_P3HTPCBM_BHJ.csv'):
    row = line.strip().split(',')
    if row[0].isdigit():
        p3ht_wavelengths.append(int(row[0]))
        p3ht_eta.append(float(row[1]))
        p3ht_k.append(float(row[2]))
p3ht_n = np.array(p3ht_eta) + 1j*np.array(p3ht_k) # complex indices of refract
ion
p3ht_q = np.array(p3ht_n) # since we are assuming that the angle of incidence
 is 0
p3ht_q = dict(zip(p3ht_wavelengths, p3ht_q))
```

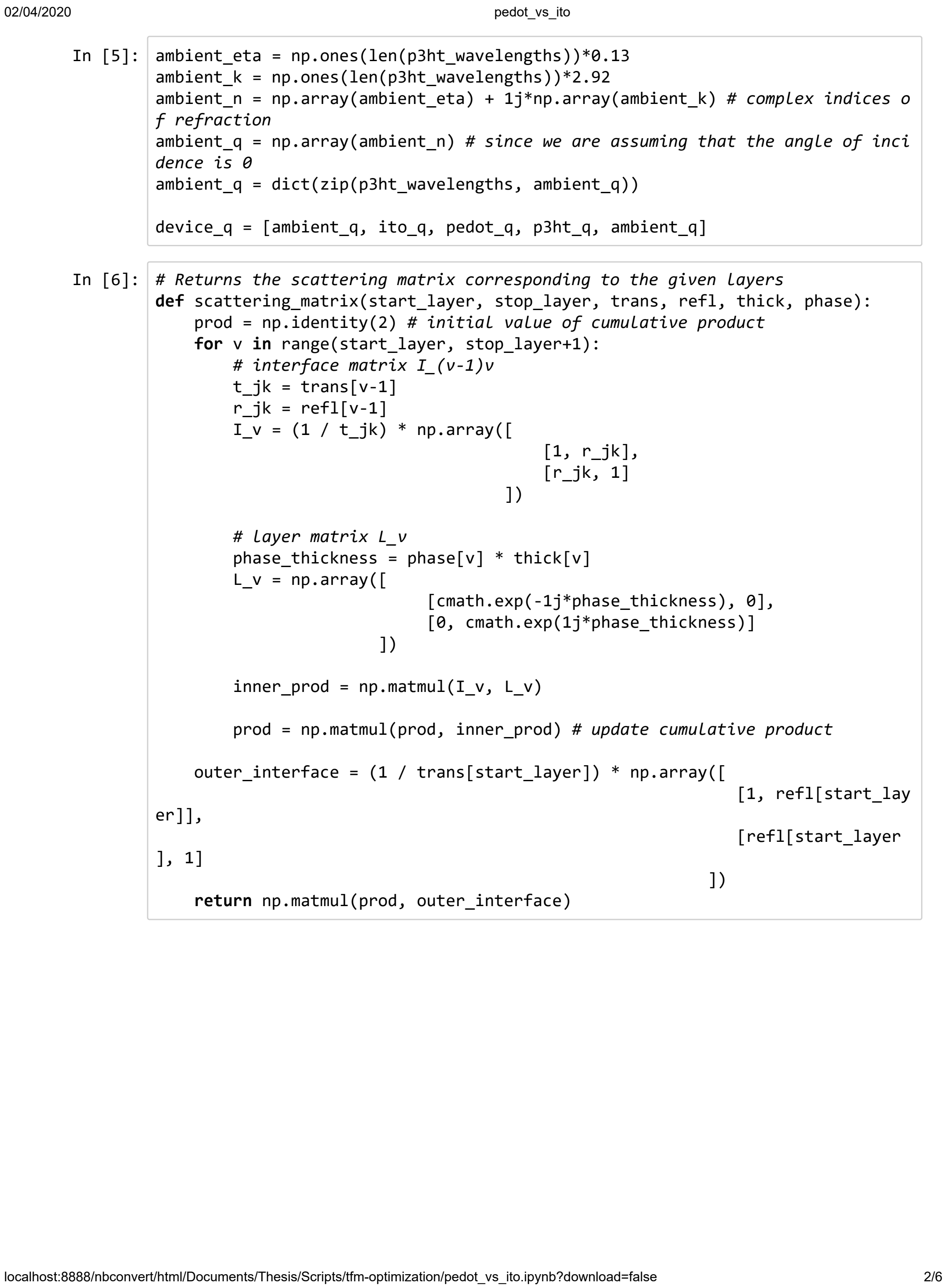

In [5]:

```
ambient_eta = np.ones(len(p3ht_wavelengths))*0.13
ambient_k = np.ones(len(p3ht_wavelengths))*2.92
ambient_n = np.array(ambient_eta) + 1j*np.array(ambient_k) # complex indices o
f refraction
ambient_q = np.array(ambient_n) # since we are assuming that the angle of inci
dence is 0
ambient_q = dict(zip(p3ht_wavelengths, ambient_q))

device_q = [ambient_q, ito_q, pedot_q, p3ht_q, ambient_q]
```

In [6]:

```
# Returns the scattering matrix corresponding to the given layers
def scattering_matrix(start_layer, stop_layer, trans, refl, thick, phase):
    prod = np.identity(2) # initial value of cumulative product
    for v in range(start_layer, stop_layer+1):
        # interface matrix I_(v-1)v
        t_jk = trans[v-1]
        r_jk = refl[v-1]
        I_v = (1 / t_jk) * np.array([
                                        [1, r_jk],
                                        [r_jk, 1]
                                    ])

        # layer matrix L_v
        phase_thickness = phase[v] * thick[v]
        L_v = np.array([
                            [cmath.exp(-1j*phase_thickness), 0],
                            [0, cmath.exp(1j*phase_thickness)]
                       ])

        inner_prod = np.matmul(I_v, L_v)

        prod = np.matmul(prod, inner_prod) # update cumulative product

    outer_interface = (1 / trans[start_layer]) * np.array([
                                                            [1, refl[start_lay
er]],
                                                            [refl[start_layer
], 1]
                                                        ])
    return np.matmul(prod, outer_interface)
```

In [7]:

```
wavelengths = pedot_wavelengths
R = [] # reflectivity
A = [] # absorbance
for lambdie in wavelengths:
    # Fresnel complex coefficients
    # t[0] corresponds to t_01 in the above theory
    t = [] # transmission
    r = [] # reflection

    for j in range(len(device_q) - 1):
        k = j+1
        t_jk = (2 * device_q[j][lambdie]) / (device_q[j][lambdie] + device_q[k
][lambdie])
        r_jk = (device_q[j][lambdie] - device_q[k][lambdie]) / (device_q[j][la
mbdie] + device_q[k][lambdie])
        t.append(t_jk)
        r.append(r_jk)

    t = np.array(t)
    r = np.array(r)
    xi = np.zeros(len(device_q), dtype=complex)
    for layer in range(len(device_q)-1):
        xi[layer] = device_q[layer][lambdie] * (2 * math.pi / lambdie)
    xi[0] = float("inf")

    S = scattering_matrix(start_layer=1, stop_layer=3, trans=t, refl=r, thick=
d, phase=xi)
    r_complex = S[0][1] / S[0][0]
    reflectivity = np.abs(r_complex)**2
    R.append(reflectivity)
    A.append(1 - reflectivity)
```

In [8]:

```
ito_device_wavelengths = wavelengths
ito_device_A = A
plt.plot(ito_device_wavelengths[100:], ito_device_A[100:])
plt.xlabel("Wavelength (nm)")
plt.ylabel("Absorption")
plt.ylim(0, 1)
plt.xlim(300, 850)

plt.show()
```

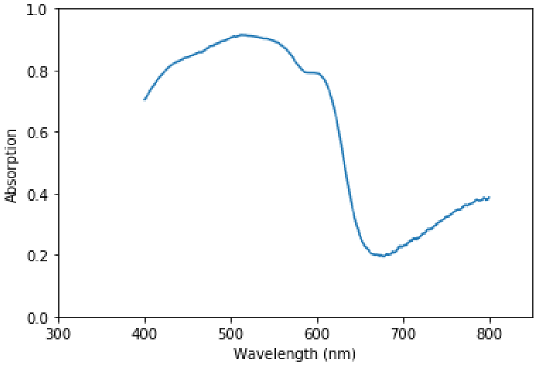

PEDOT:PSS Anode

In [17]:

```
d = [float("inf"), 165, 110, float("inf")]

pedot_anode_eta = []
pedot_anode_k = []
pedot_anode_wavelengths = []
for line in open('data/nk_PEDOT.csv'):
    row = line.strip().split(',')
    if row[0].isdigit():
        pedot_anode_wavelengths.append(int(row[0]))
        pedot_anode_eta.append(float(row[1]))
        pedot_anode_k.append(float(row[2]))
pedot_anode_n = np.array(pedot_anode_eta) + 1j*np.array(pedot_anode_k) # compl
ex indices of refraction
pedot_anode_q = pedot_anode_n # since we are assuming that the angle of incide
nce is 0
pedot_anode_q = dict(zip(pedot_anode_wavelengths, pedot_anode_q))
```

In [18]:

```
pedot_device_q = [ambient_q, pedot_anode_q, p3ht_q, ambient_q]
```

In [19]:

```
wavelengths = pedot_wavelengths
R = []
A = []
for lambdie in wavelengths:
    # Fresnel complex coefficients
    # t[0] corresponds to t_01 in the above theory
    t = [] # transmission
    r = [] # reflection

    for j in range(len(pedot_device_q) - 1):
        k = j+1
        t_jk = (2 * pedot_device_q[j][lambdie]) / (pedot_device_q[j][lambdie]
+ pedot_device_q[k][lambdie])
        r_jk = (pedot_device_q[j][lambdie] - pedot_device_q[k][lambdie]) / (pe
dot_device_q[j][lambdie] + pedot_device_q[k][lambdie])
        t.append(t_jk)
        r.append(r_jk)

    t = np.array(t)
    r = np.array(r)
    xi = np.zeros(len(pedot_device_q), dtype=complex)
    for layer in range(len(pedot_device_q)-1):
        xi[layer] = pedot_device_q[layer][lambdie] * (2 * math.pi / lambdie)
    xi[0] = float("inf")

    S = scattering_matrix(start_layer=1, stop_layer=2, trans=t, refl=r, thick=
d, phase=xi)
    r_complex = S[0][1] / S[0][0]
    reflectivity = np.abs(r_complex)**2
    R.append(reflectivity)
    A.append(1 - reflectivity)
```

In [20]:

```
plt.plot(wavelengths[100:], A[100:])
plt.xlabel("Wavelength (nm)")
plt.ylabel("Absorption")
plt.ylim(0, 1)
plt.xlim(300, 850)
plt.show()
```

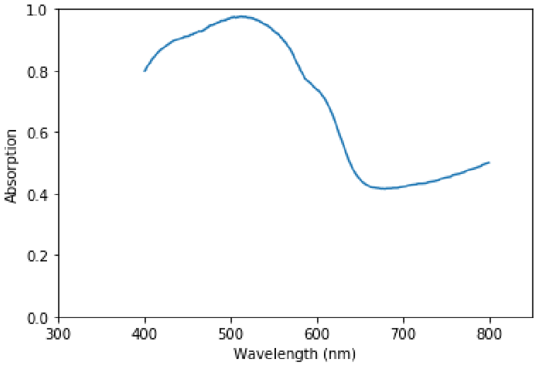

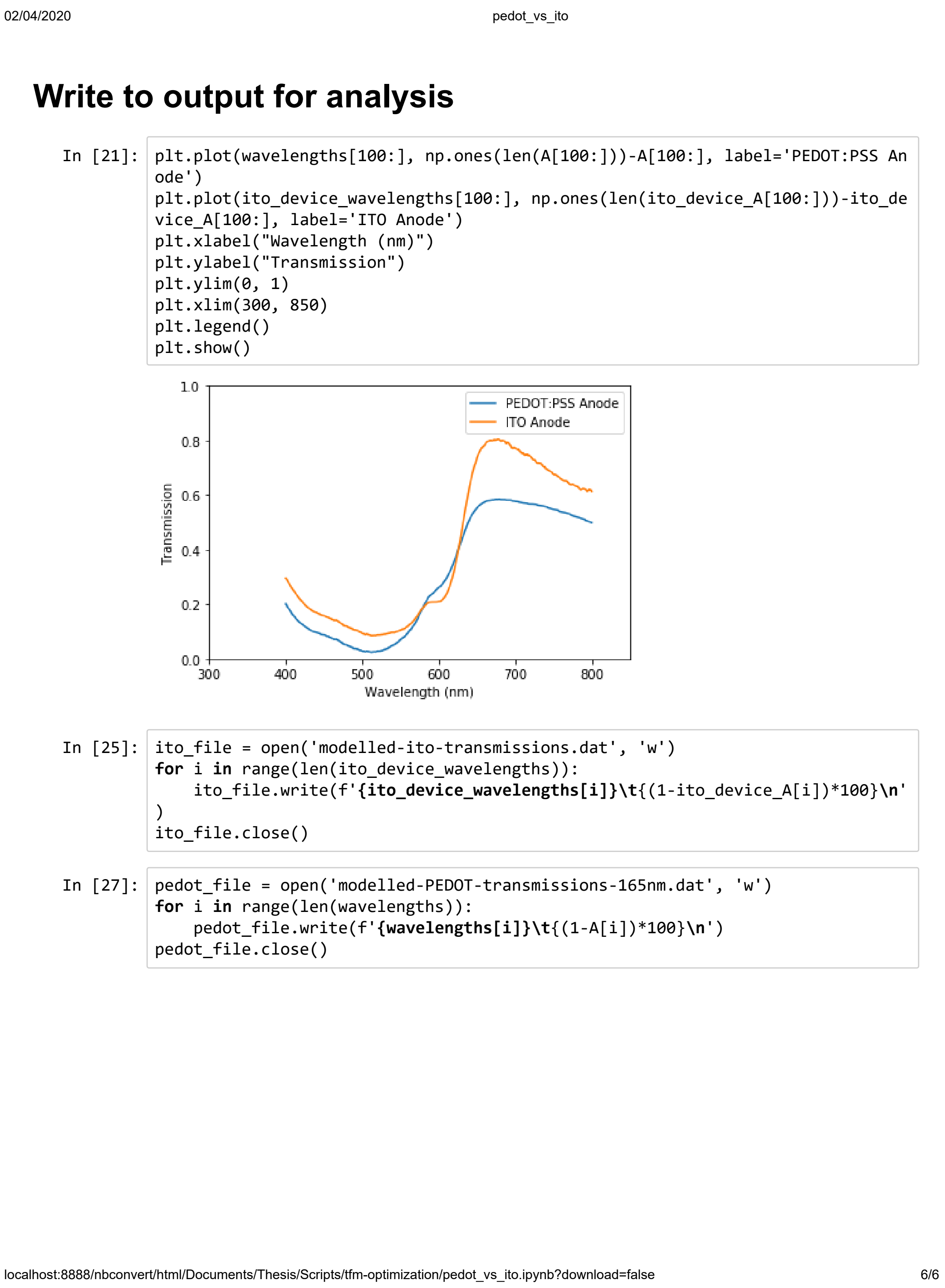

02/04/2020 pedot_vs_ito

Write to output for analysis

In [21]:

```
plt.plot(wavelengths[100:], np.ones(len(A[100:]))-A[100:], label='PEDOT:PSS An
ode')
plt.plot(ito_device_wavelengths[100:], np.ones(len(ito_device_A[100:]))-ito_de
vice_A[100:], label='ITO Anode')
plt.xlabel("Wavelength (nm)")
plt.ylabel("Transmission")
plt.ylim(0, 1)
plt.xlim(300, 850)
plt.legend()
plt.show()
```

In [25]:

```
ito_file = open('modelled-ito-transmissions.dat', 'w')
for i in range(len(ito_device_wavelengths)):
    ito_file.write(f'{ito_device_wavelengths[i]}\t{(1-ito_device_A[i])*100}\n'
)
ito_file.close()
```

In [27]:

```
pedot_file = open('modelled-PEDOT-transmissions-165nm.dat', 'w')
for i in range(len(wavelengths)):
    pedot_file.write(f'{wavelengths[i]}\t{(1-A[i])*100}\n')
pedot_file.close()
```

localhost:8888/nbconvert/html/Documents/Thesis/Scripts/tfm-optimization/pedot_vs_ito.ipynb?download=false 6/6